Nuclear Physics B113 (1976) 53–92

RHO PRODUCTION BY VIRTUAL PHOTONS

P. JOOS, A. LADAGE, H. MEYER, P. STEIN *, G. WOLF and S. YELLIN **
Deutsches Elektronen-Synchrotron DESY, Hamburg

C.K. CHEN ***, J. KNOWLES, D. MARTIN, J.M. SCARR, I.O. SKILLICORN and K. SMITH
University of Glasgow, Glasgow

C. BENZ, G. DREWS, D. HOFFMANN ‡, J. KNOBLOCH, W.KRAUS, H.NAGEL, E. RABE, C. SANDER, W.-D. SCHLATTER ‡‡, H. SPITZER and K. WACKER
II. Institut für Experimentalphysik der Universität Hamburg

Received 26 April 1976

The reaction $\gamma_V p \to p\pi^+\pi^-$ was studied in the W, Q^2 region 1.3–2.8 GeV, 0.3–1.4 GeV^2 using the streamer chamber at DESY. A detailed analysis of rho production *via* $\gamma_V p \to \rho^0 p$ is presented. Near threshold rho production has peripheral and non-peripheral contributions of comparable magnitude. At higher energies ($W > 2$ GeV) the peripheral component is dominant. The Q^2 dependence of $\sigma(\gamma_V p \to \rho^0 p)$ follows that of the rho propagator as predicted by VDM. The slope of $d\sigma/dt$ at $\langle Q^2 \rangle = 0.4$ and 0.8 GeV^2 is within errors equal to its value at $Q^2 = 0$. The overall shape of the ρ^0 is t dependent as in photoproduction, but is independent of Q^2. The decay angular distribution shows that longitudinal rhos dominate in the threshold region. At higher energies transverse rhos are dominant. Rho production by transverse photons proceeds almost exclusively by natural parity exchange, $\sigma_T^N \geqslant (0.83 \pm 0.06)\,\sigma_T$ for $2.2 < W < 2.8$ GeV. The s-channel helicity-flip amplitudes are small compared to non-flip amplitudes. The ratio $R = \sigma_L/\sigma_T$ was determined assuming s-channel helicity conservation. We find $R = \xi^2 Q^2/M_\rho^2$ with $\xi^2 \approx 0.4$ for $\langle W \rangle = 2.45$ GeV. Interference between rho production amplitudes from longitudinal and transverse photons is observed. With increasing energy the phase between the two amplitudes decreases. The observed features of rho electroproduction are consistent with a dominantly diffractive production mechanism for $W > 2$ GeV.

* On leave of absence from Cornell University, Ithaca, NY, USA.
** Now at University of California, Santa Barbara, California, USA.
*** Now at Argonne National Laboratory, Argonne, Ill., USA.
‡ Now at Technische Hochschule Aachen, III. Physikalisches Institut A, D51 Aachen.
‡‡ Now at CERN, Geneva.

1. Introduction

This is one of several final reports on an experiment which used the DESY streamer chamber to study the hadronic final states produced in electron-proton scattering. The experiment covered hadron c.m.s. energies W between threshold and 2.8 GeV and values of the photon mass squared, $-Q^2$ from -0.3 to -1.4 GeV^2. The experimental set-up had 4π acceptance for detection of charged hadrons. In this paper we present our final results on rho production by virtual photons *via*

$$\gamma_V p \to \rho^0 p \,. \tag{1}$$

Preliminary results obtained with a fraction of the data on multiplicities, rho and Δ^{++} production have already been published [1–4].

Reaction (1) provides the opportunity to measure quasielastic virtual photon-nucleon scattering as a function of the photon mass. At $Q^2 = 0$ rho production has the characteristics of a diffractive process (for $W \gtrsim 2$ GeV); i.e. the production cross section is approximately constant as a function of energy, it is peripheral ($d\sigma/dt \sim \exp At$ with $A = 6$–8 GeV^{-2}), and is dominated by natural parity isoscalar exchange. It is one of the aims of this experiment to see whether rho production by *virtual* photons is also a dominantly diffractive process or whether other production mechanisms become important with increasing Q^2. To this end we have measured the W and t dependence of the rho production cross section as a function of Q^2. The Q^2 dependence of the cross section provides a direct test of the Vector Dominance Model (VDM), while the slope of $d\sigma/dt$ can show whether the interaction radius of the photon changes with Q^2.

An analysis of the rho-decay distribution allows us to study the spin states involved. From this we can (i) obtain a lower limit to the natural parity exchange cross section for production of transverse rhos; (ii) test for s-channel helicity conservation (SCHC), which holds well in photoproduction; (iii) determine the ratio of the cross sections for rho production by transverse and longitudinal photons, respectively.

The paper is organized as follows: first we review the experimental procedure. In sect. 3 we describe the general characteristics of the reaction $\gamma_V p \to p\pi^+\pi^-$, i.e. channel cross sections and mass distributions. In sect. 4 we discuss the ρ mass shape, the ρ production cross section as a function of W, Q^2 and t, and the ρ decay distributions. The conclusions are given in sect. 5.

2. Experimental procedure

A detailed description of the setup and the event analysis has been given in ref. [2]. A 7.2 GeV electron beam was directed onto a 9 cm long liquid hydrogen target inside the streamer chamber. The streamer chamber which had a length of 1 m was placed in a magnetic field of 18 kG. Two arrays of trigger counters, lucite Čerenkov counters and lead scintillator sandwich shower counters detected the scattered elec-

tron. About 70% of the data were taken with a proportional wire chamber added to each of the two detector arms [5]. The proportional chambers measured the x and y coordinates of the scattered electron behind the magnet. This improved the momentum and angular resolution by more than a factor of two as compared with earlier runs where the electron track was measured in the streamer chamber only. With the proportional chambers the average error on the electron momentum was $\Delta p = \pm p^2/p_{\mathrm{MDM}}$ with $p_{\mathrm{MDM}} \simeq 250$ GeV/c; the error on the scattering angle was about ±1 mrad.

Approximately 400 000 pictures were taken with a total flux of $4 \cdot 10^{12}$ electrons incident on the target. The photographs were scanned twice and ambiguities were resolved in a third scan. The event analysis was similar to that used in bubble chamber experiments. The geometrical and kinematical reconstruction was done using the programs THRESH and GRIND [6]. A total of ~9100 elastic and ~37 000 inelastic ep scattering events were obtained *.

Rho meson production *via* reaction (1) was studied in the final state

$$\mathrm{ep} \to \mathrm{ep}\pi^+\pi^- \,. \tag{2}$$

The events selected for reaction (2) were required to give a 4C fit ($\chi^2 < 37$) consistent with the observed track ionization. For 10% of the events of reaction (2) one track was obscured by the target box or by flares. These events had to give a 1C fit ($\chi^2 < 28$); the obscured track was recovered by the fit. A total of 7383 events were found in the kinematical region $1.3 < W < 2.8$ GeV, $0.3 < Q^2 < 1.4$ GeV^2 which satisfied these selection criteria.

Two independent Monte Carlo programs, which simulated the event production and detection, were used to check the fit procedure and event selection and to determine the radiative corrections. The Monte Carlo events were processed through THRESH and GRIND in the same way as the measured events. The contamination of events from other reactions giving an acceptable fit for reaction (2) was found to be smaller than 5%. The radiative corrections were estimated in the peaking approximation. The corrections amount typically to a +22% contribution from external and internal bremsstrahlung and a −7% contribution from vertex and propagator effects [7] (see ref. [8] for details).

Cross sections were determined by normalizing the total number of events (after correcting for acceptance and radiative effects) to the total inelastic ep cross section measured in a single arm experiment [9]. The errors given below are statistical only. A systematic uncertainty of ±10% has to be added which covers the uncertainties from event selection (5%), radiative corrections (4%) and cross section normalization (7%).

* 2-prong events were analyzed on 50% of the film only.

3. General characteristics of the reaction $\gamma_V p \to p\pi^+\pi^-$

3.1. Definition of the cross section

In the notation of Hand [10] the differential cross section $d^2\sigma(f)/dQ^2\,dW$ for electroproduction of a final state f is expressed in terms of the cross section $\sigma_T(f)$ and $\sigma_L(f)$ for production of f by scattering of transverse and longitudinal virtual photons on protons:

$$\frac{d\sigma(f)}{dQ^2 dW} = \frac{\pi}{EE'}\,\frac{W}{m_p}\,\Gamma_T\{\sigma_T(Q^2, W, f) + \epsilon\sigma_L(Q^2, W, f)\}\,, \tag{3}$$

where E, E' are the energies of the incident and scattered electron, m_p is the mass of the proton, Γ_T measures the flux of transverse photons,

$$\Gamma_T = \frac{\alpha}{4\pi^2}\,\frac{E'}{E}\,\frac{W^2 - m_p^2}{m_p Q^2}\,\frac{1}{1-\epsilon} \tag{4}$$

with

$$\epsilon = \left[1 + 2\,\frac{\nu^2 + Q^2}{4EE' - Q^2}\right]^{-1}, \quad \text{for } Q^2 >> m_e^2\,, \quad \nu = E - E'\,. \tag{5}$$

For the majority of our events the polarization parameter ϵ lies in the range 0.85–0.95. The value of ϵ is fixed for a given Q^2 and W. Therefore no model independent separation of σ_T and σ_L can be made in this experiment. The $\gamma_V p$ cross section is defined as

$$\sigma(Q^2, W) \equiv \sigma_T(Q^2, W) + \epsilon\sigma_L(Q^2, W)\,. \tag{6}$$

3.2. W and Q^2 dependence of the channel cross section

Fig. 1 gives the W dependence of the cross section for

$$\gamma_V p \to p\pi^+\pi^- \tag{7}$$

in different intervals of Q^2. The production features are similar to those observed in photoproduction [11, 12] (shown by the open points): namely a sharp rise at threshold, a broad maximum between 1.4 and 1.8 GeV followed by slow decrease at higher energies. The Q^2 dependence of the cross section is shown in fig. 2 for various regions of W. For comparison the Q^2 dependence of the total inelastic $\gamma_V p$ cross section [9] normalized to $\sigma(\gamma_V p \to p\pi^+\pi^-)$ at $Q^2 = 0$ [12] is also given (dashed curves). The cross section for reaction (7) is seen to drop somewhat faster with Q^2 than the total cross section. As we shall see below (subsect. 3.3) this is caused by the rapid decrease of Δ^{++} and ρ^0 production with Q^2. Table 1 provides a complete listing of the cross section in small intervals of W and Q^2.

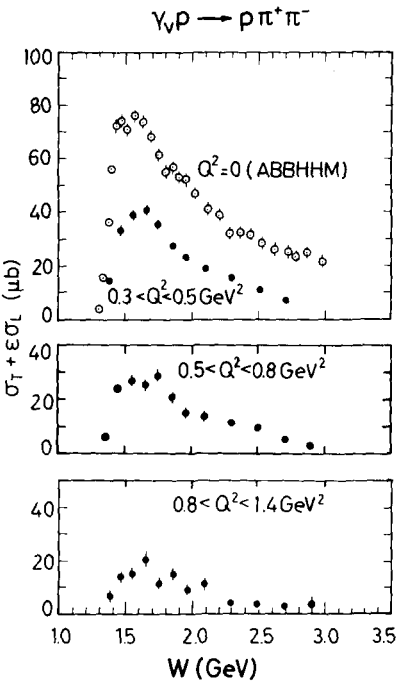

Fig. 1. Channel cross section $\sigma(\gamma_V p \rightarrow p\pi^+\pi^-)$ as a function of W for three different intervals of Q^2. The open points are results at $Q^2 = 0$ of the ABBHHM Collaboration as quoted in ref. [12].

3.3. Mass distributions and resonance production

The $p\pi^+$, $p\pi^-$ and $\pi^+\pi^-$ mass distributions are shown in figs. 3–5 for different Q^2 and W intervals. Below 1.7 GeV $\Delta^{++}(1236)$ production dominates. Above the rho threshold (W = 1.7 GeV) rho production shows up and becomes the dominant channel for $W > 2$ GeV. The rho signal is seen more clearly when a cut on the momentum transfer ($|t|_{p/p} < 0.5$ GeV^2) is applied (see shaded parts of figs. 4 and 5). As in photoproduction the rho mass shape is skewed: it is enhanced at the low mass side and depressed above the mass of the rho. The t_{min} cut-off plays only a minor role in this context. We shall discuss the rho shape below (subsect. 4.1). As seen from the $M_{p\pi^-}$ distributions the production of $\Delta^0(1236)$ is small at all energies.

The cross sections for Δ^{++}, Δ^0 and ρ^0 production in reaction (7) were determined by a maximum likelihood fit to the Dalitz plot density $dN(M^2_{p\pi^+}, M^2_{\pi^+\pi^-})$ [13]:

$$dN(M^2_{p\pi^+}, M^2_{\pi^+\pi^-}) = [a_{\Delta^{++}} F_{\Delta^{++}}(M_{p\pi^+}) + a_{\Delta^0} F_{\Delta^0}(M_{p\pi^-}) + a_\rho F_\rho(M_{\pi^+\pi^-})\, W(\cos\theta_H) + a_{ps} F_{ps}]\, dM^2_{p\pi^+}\, dM^2_{\pi^+\pi^-} \,. \quad (8)$$

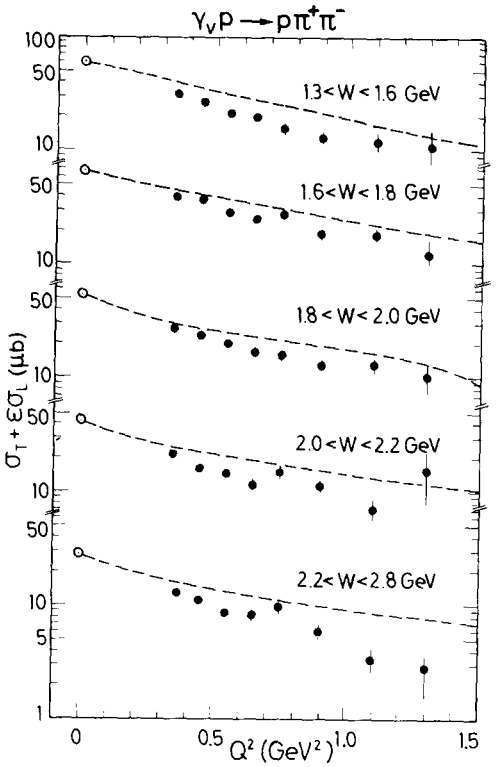

Fig. 2. Channel cross section $\sigma(\gamma_V p \rightarrow p\pi^+\pi^-)$ as a function of Q^2 for five intervals of W. The open points at $Q^2 = 0$ were taken from ref. [12]. The curves represent the Q^2 dependence of the total inelastic $\gamma_V p$ cross section, normalized to $\sigma(\gamma p \rightarrow p\pi^+\pi^-)$ at $Q^2 = 0$. The curves were obtained from a fit to the data of ref. [9].

The a's which appear in eq. (8) are fit parameters and measure the size of the Δ^{++}, Δ^0, ρ^0 and phase space like background contributions. The F's describe normalized relativistic Breit-Wigner distributions (for details see ref. [8]), e.g.

$$F_\rho = B_\rho / I_\rho \ ,$$

$$B_\rho = \frac{M_{\pi^+\pi^-}}{q(M_{\pi^+\pi^-})} \ \frac{\Gamma(M_{\pi^+\pi^-})}{(M_\rho^2 - M_{\pi^+\pi^-}{}^2)^2 + M_\rho^2 \Gamma^2(M_{\pi^+\pi^-})} \ , \tag{9}$$

where q measures the pion momentum in the $\pi^+\pi^-$ rest frame. The normalization constant I_ρ is obtained from an integration over the Dalitz plot

$$I_\rho = \int B_\rho \ \mathrm{d}M^2_{\mathrm{p}\pi^+} \, \mathrm{d}M^2_{\pi^+\pi^-} \ , \tag{10}$$

Table 1
Reaction $\gamma_V p \to p\pi^+\pi^-$; channel cross section $\sigma_T + \epsilon\sigma_L$ (μb)

Q^2 (GeV^2) \ W (GeV)	1.3–1.4	1.4–1.5	1.5–1.6	1.6–1.7	1.7–1.8
0 (Ref. [12])	26	72.1	73.0	71.2	61.0
0.3–0.4	13.6 ± 1.8	40.3 ± 3.0	40.9 ± 3.0	42.6 ± 3.0	36.8 ± 2.8
0.4–0.5	14.7 ± 1.9	26.8 ± 2.5	37.3 ± 2.8	38.8 ± 2.8	35.0 ± 2.7
0.5–0.6	7.2 ± 1.5	23.4 ± 2.6	32.1 ± 3.0	27.6 ± 2.7	29.3 ± 2.8
0.6–0.7	6.4 ± 1.7	24.8 ± 3.3	26.8 ± 3.3	24.4 ± 3.1	26.6 ± 3.3
0.7–0.8	3.3 ± 1.5	21.7 ± 3.7	21.2 ± 3.6	24.3 ± 3.7	31.7 ± 4.3
0.8–1.0	4.0 ± 1.5	16.3 ± 3.0	19.4 ± 3.1	17.8 ± 2.8	18.3 ± 2.8
1.0–1.2	5.6 ± 2.6	15.4 ± 4.3	15.0 ± 3.9	21.8 ± 4.6	13.7 ± 3.6
1.2–1.4	10.3 ± 6.1	10.1 ± 5.1	12.1 ± 5.5	21.0 ± 8.3	3.3 ± 2.3
Q^2 (GeV^2) \ W (GeV)	1.8–2.0	2.0–2.2	2.2–2.5	2.5–2.8	2.8–3.0
0 (Ref. [12])	53	42	32.6	25.5	23.5
0.3–0.4	27.1 ± 1.6	21.7 ± 1.6	15.7 ± 1.4	9.9 ± 1.9 [a]	
0.4–0.5	24.0 ± 1.4	16.3 ± 1.3	13.3 ± 1.0	7.9 ± 1.0	2.3 ± 0.8
0.5–0.6	20.6 ± 1.6	14.5 ± 1.4	9.6 ± 1.1	7.2 ± 1.1	5.2 ± 1.3
0.6–0.7	17.2 ± 1.8	11.7 ± 1.5	11.4 ± 1.4	5.2 ± 1.1	4.0 ± 1.4
0.7–0.8	15.9 ± 2.1	14.5 ± 2.0	11.5 ± 1.7	7.9 ± 1.6	2.0 ± 1.1
0.8–1.0	13.0 ± 1.6	11.4 ± 1.6	8.4 ± 1.2	3.3 ± 0.9	2.8 ± 1.2
1.0–1.2	13.1 ± 2.2	7.2 ± 1.6	4.4 ± 1.2	2.2 ± 0.9	3.1 ± 1.6
1.2–1.4	10.3 ± 3.1	15.2 ± 7.5	1.3 ± 1.0	4.5 ± 2.5	5.3 ± 4.2

[a] For $0.35 < Q^2 < 0.4$ GeV^2.

where the integration limits depend on the W value of the particular event.

In case of the rho, the Breit-Wigner is multiplied by the factor $(M_\rho/M_{\pi^+\pi^-})^n$ where n is a fit parameter that determines the ρ shape. Also, the polar decay angular distribution, $W(\cos\theta_H)$, for rho events in the helicity system was included in the fit since the experimental $\cos\theta_H$ distribution is strongly affected by contributions from Δ^{++} and Δ^0 production. In terms of the ρ density matrix element r_{00}^{04} (see ref. [14] and the appendix of this paper for details):

$$W(\cos\theta_H) = \tfrac{3}{4}\{1 - r_{00}^{04} + (3r_{00}^{04} - 1)\cos^2\theta_H\}\,. \tag{11}$$

The quantity F_{ps} describes events which are distributed in the Daltiz plot according to phase space. F_{ps} is a constant and is normalized in the same manner as e.g. F_ρ.

In a first set of fits the ρ mass and width were treated as free parameters. Within errors the same mass and width, $M_\rho = 0.78$ GeV, $\Gamma_\rho = 0.15$ GeV were obtained in all

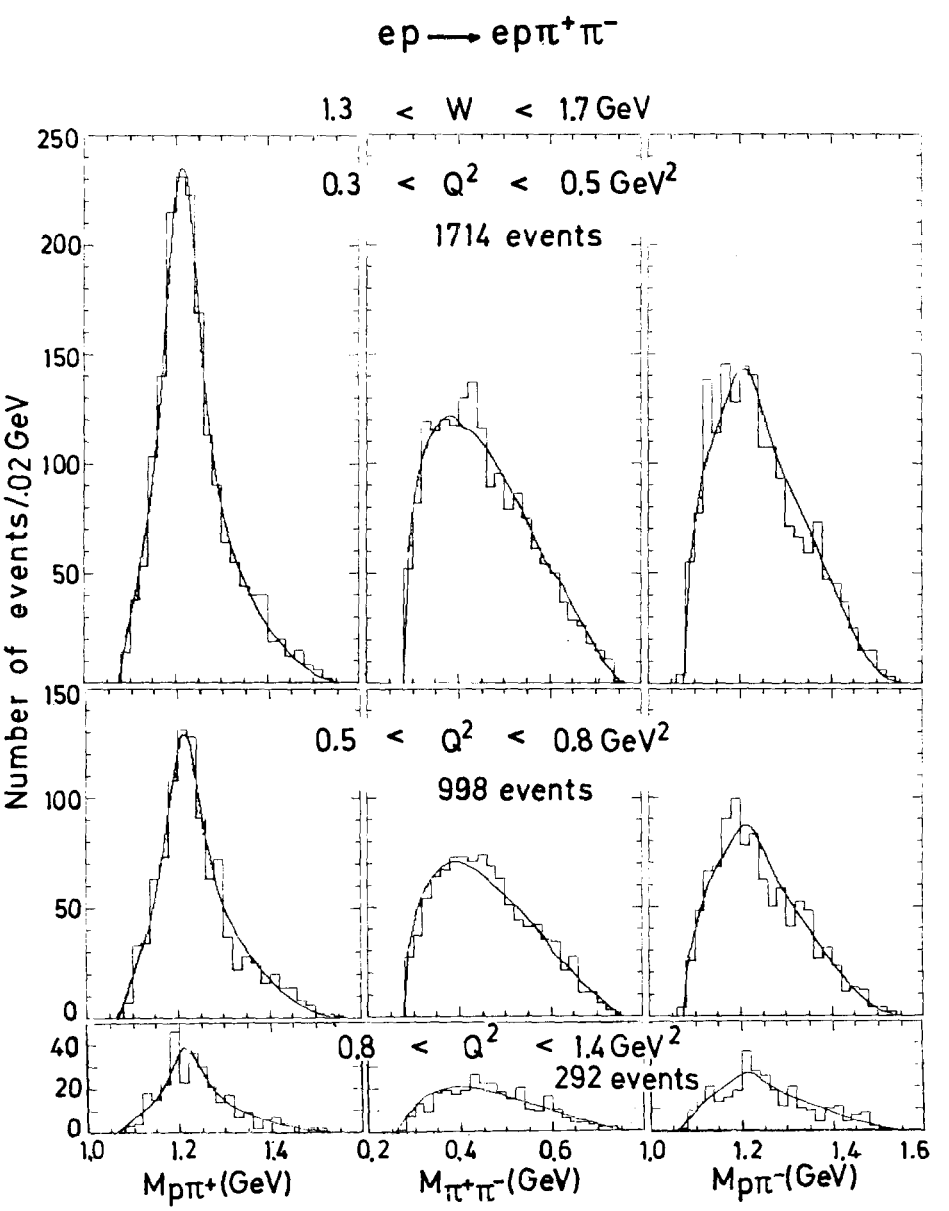

Fig. 3. Distributions of the effective masses $M_{p\pi^+}$, $M_{\pi^+\pi^-}$, $M_{p\pi^-}$ from the reaction $ep \to ep\pi^+\pi^-$ for $1.3 < W < 1.7$ GeV and three Q^2 intervals. The curves are taken from a fit to the Dalitz plot. Typically 1.7% [5.8%] of the events with $1.3 < W < 1.7$ GeV ($1.7 < W < 2.8$ GeV) gave two (ambiguous) fits of reaction (2) per event. In figs. 3–5 we have plotted both fits with unit weight each. Hence the actual number of events is smaller by 1.7–5.8% than the numbers given in the figures.

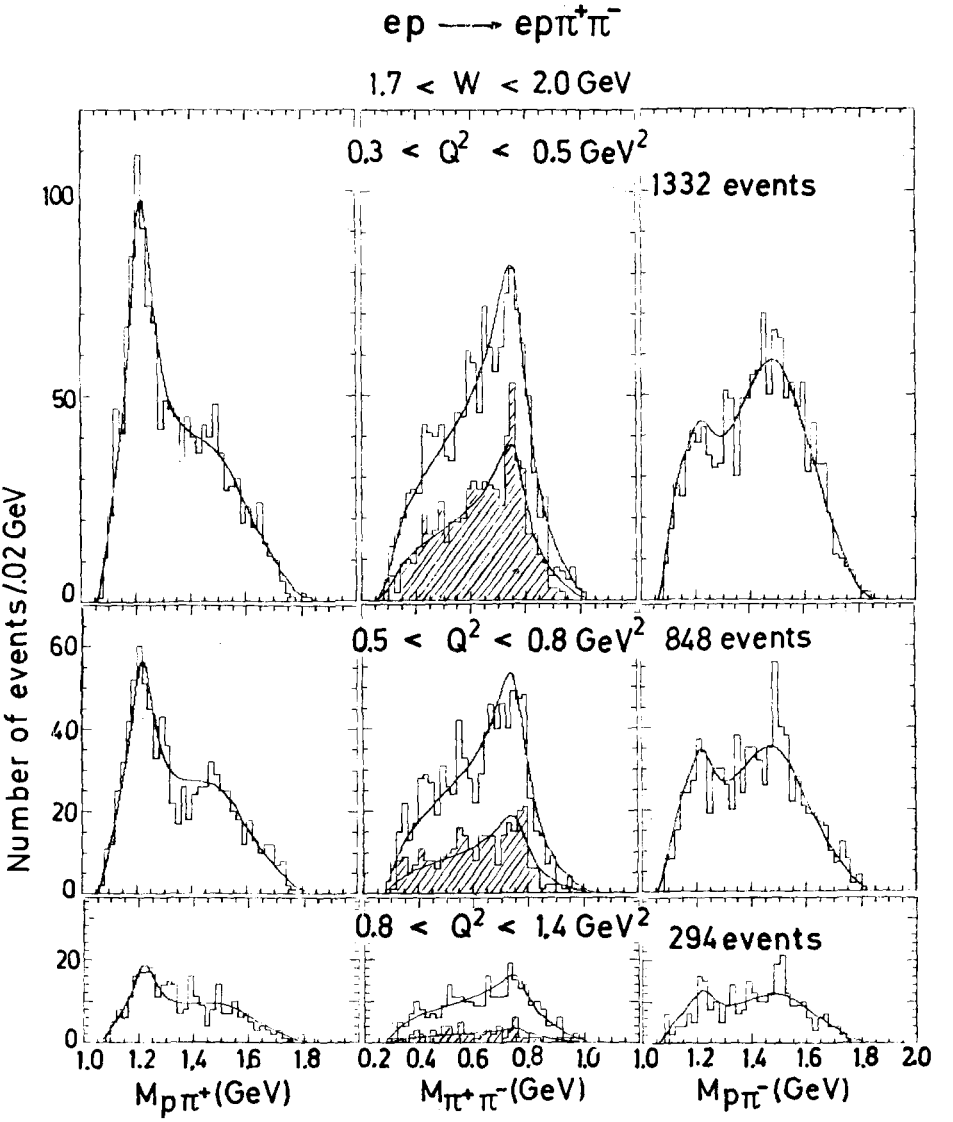
ep ⟶ epπ⁺π⁻
1.7 < W < 2.0 GeV
0.3 < Q² < 0.5 GeV²
1332 events
0.5 < Q² < 0.8 GeV²
848 events
0.8 < Q² < 1.4 GeV²
294 events
Number of events/.02 GeV
Mpπ⁺(GeV)
Mπ⁺π⁻(GeV)
Mpπ⁻(GeV)

Fig. 4a.

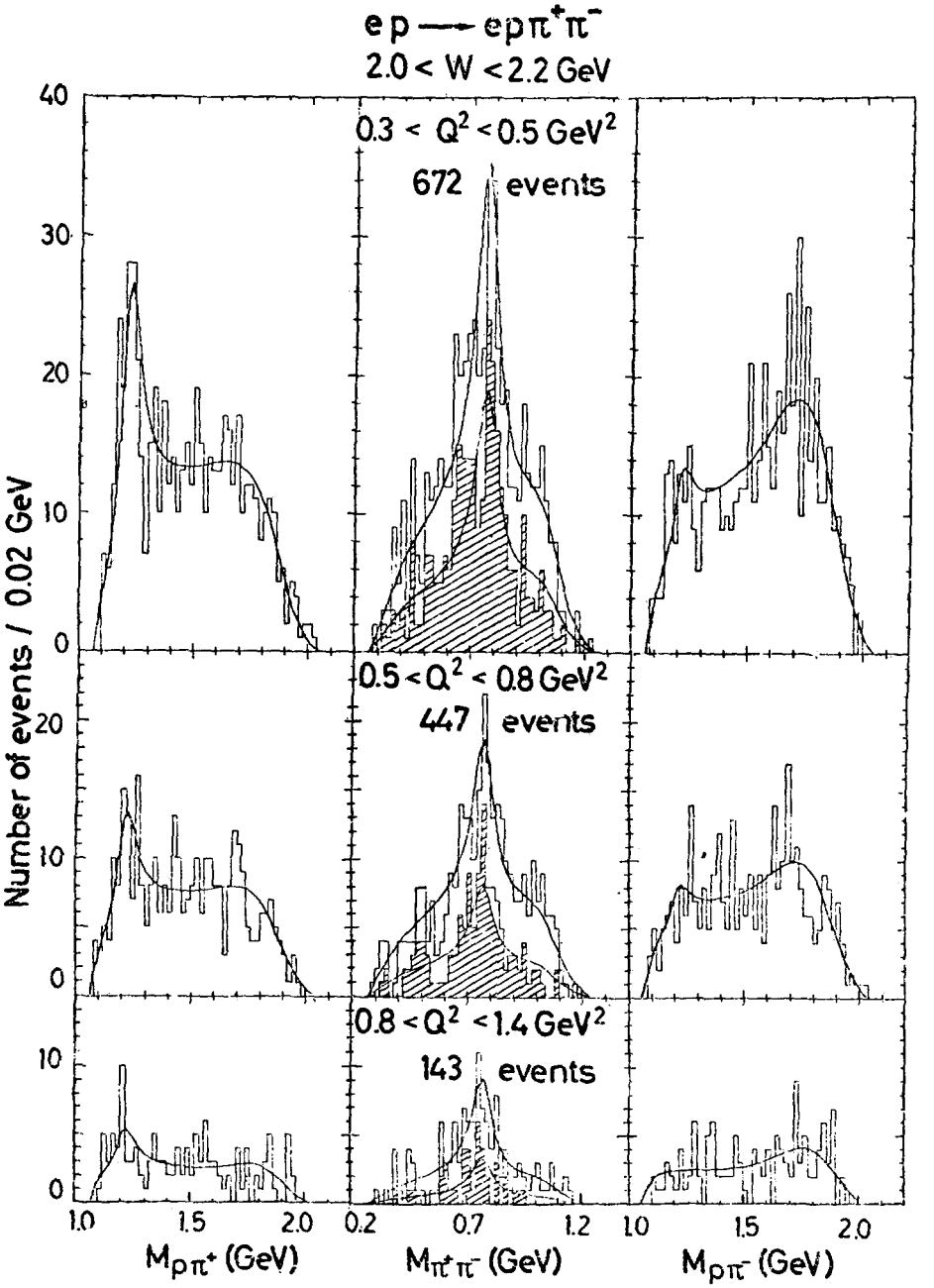
ep → epπ⁺π⁻
2.0 < W < 2.2 GeV
0.3 < Q² < 0.5 GeV²
672 events
0.5 < Q² < 0.8 GeV²
447 events
0.8 < Q² < 1.4 GeV²
143 events
Number of events / 0.02 GeV
Mpπ⁺ (GeV)
Mπ⁺π⁻ (GeV)
Mpπ⁻ (GeV)

Fig. 4b.

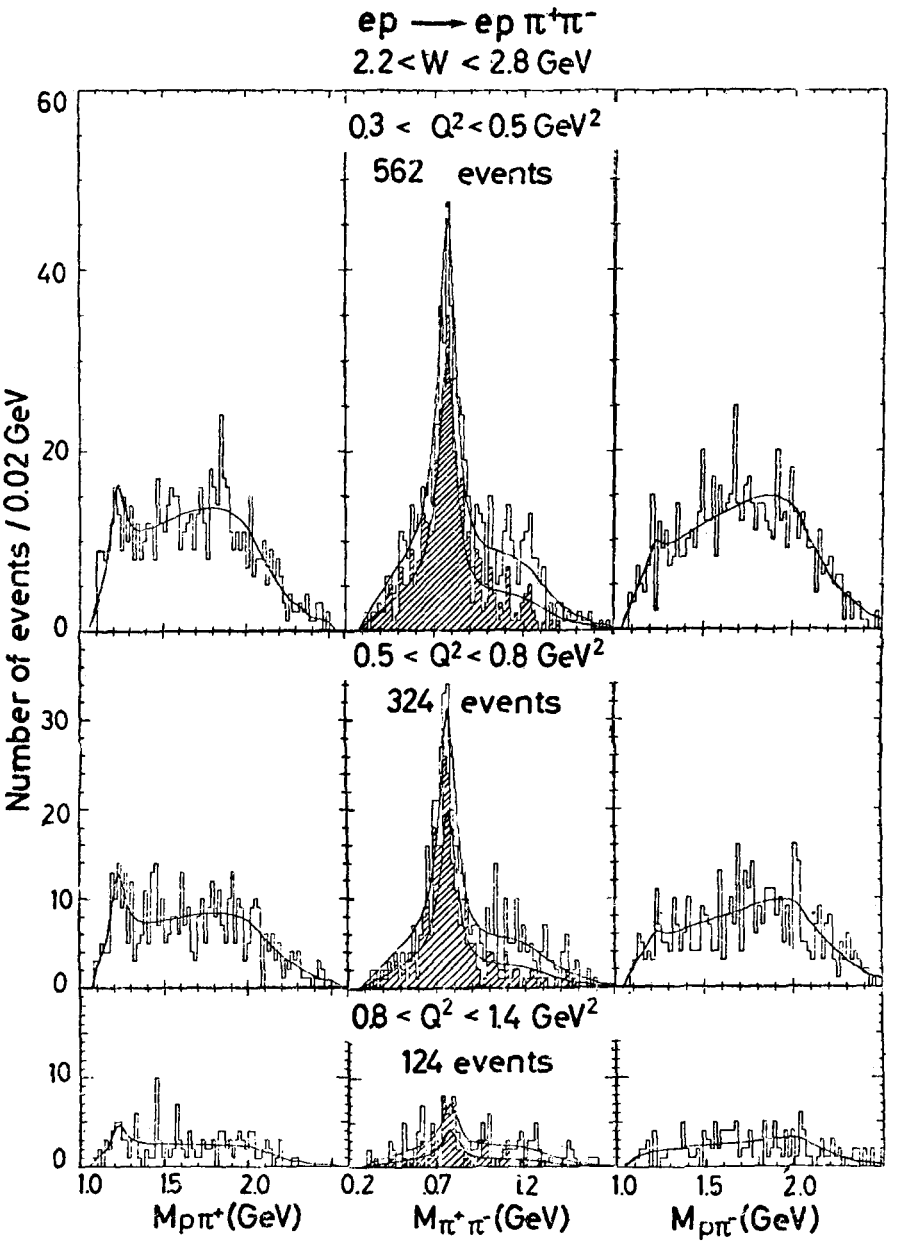

Fig. 4c.

Fig. 4. $M_{p\pi^+}$, $M_{\pi^+\pi^-}$ and $M_{p\pi^-}$ distributions for different W and Q^2 intervals. The shaded $M_{\pi^+\pi^-}$ distributions are for events with $|t| < 0.5$ GeV^2 (where $|t|$ is the 4-momentum transfer squared from γ_V to rho). The curves are from the Dalitz plot fit. (a) $1.7 < W < 2.0$ GeV. (b) $2.0 < W < 2.2$ GeV. (c) $2.2 < W < 2.8$ GeV.

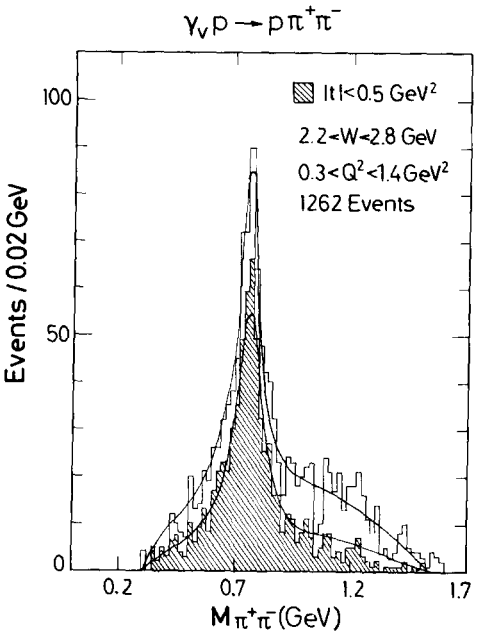

Fig. 5. $M_{\pi^+\pi^-}$ distribution for $2.2 < W < 2.8$ GeV and $0.3 < Q^2 < 1.4$ GeV^2. The curves are from the Dalitz plot fit.

$W - Q^2$ intervals. The fits were then repeated with M_ρ, Γ_ρ fixed at these values. The resulting values of n are given in subsect. 4.1.

The fits describe the mass distributions well as is demonstrated by the curves in figs. 3–5. The fitted fractions of Δ^{++}, Δ^0 and ρ^0 production and the phase space contribution are listed in table 2 together with the fitted value of r_{00}^{04}. For comparison the corresponding photoproduction results are also given. The *relative* contribution of Δ^{++} to reaction (7) is found to be essentially independent of Q^2. The amount of Δ^0 production is smaller by a factor of 5–10 than Δ^{++} production. The ρ^0 fraction decreases with Q^2 (by a factor of 2 between $Q^2 = 0$ and ~1 GeV^2 at $W \approx 2.5$ GeV).

The background fraction is larger than at $Q^2 = 0$ by a factor of 1.5–2.0 on the average. We find this an interesting feature of reaction (7) for the following reason. In photoproduction $p\pi^+\pi^-$ is the final state with the largest cross section (for $W \gtrsim 1.7$ GeV). Its size is determined essentially by the two-body channels $\pi^-\Delta^{++}$ and $\rho^0 p$; the background contribution is small (~20%). In contrast, electroproduction of structureless phase-space like background becomes comparable in magnitude to ρ production for $2 < W < 2.8$ GeV and $Q^2 \sim 1$ GeV^2. The Q^2 dependence of the cross section for "phase space" production (which can be reconstructed from table 2) is similar to the Q^2 dependence of the total inelastic $\gamma_V p$ cross section, i.e. the background shows the same weak decrease with increasing Q^2 as the total inelastic $\gamma_V p$ cross section.

Table 2
Reaction $\gamma_V p \to p\pi^+\pi^-$; percentages $a_{\Delta^{++}}$, a_{Δ^0}, a_ρ, a_{ps} of Δ^{++}, Δ^0, ρ and phase space production, and the ρ^0 density matrix element r_{00}^{04} as obtained from maximum likelihood fits to the Dalitz plot; the third column gives the polarization parameter ϵ; the last column gives the channel cross section.

W (GeV)	Q^2 (GeV^2)	ϵ	$a_{\Delta^{++}}$	a_{Δ^0}	a_ρ	a_{ps}	r_{00}^{04}	$\sigma(\gamma_V p \to p\pi^+\pi^-)$ (μb)
1.3–1.7	0	0	70 ± 3 [a]	10 ± 4 [a]		20 ± 5 [a]		63 [c]
	0.3–0.5	0.99	64 ± 4	9 ± 3		27 ± 9		31.9 ± 1.0
	0.5–0.8	0.98	54 ± 5	12 ± 3		34 ± 8		20.3 ± 0.8
	0.8–1.4	0.97	56 ± 8	17 ± 5		27 ± 16		14.1 ± 1.3
1.7–2.0	0	0	32 ± 2 [a]	3 ± 2 [a]	49 ± 5 [d]	16 ± 4 [d]		55 [c]
	0.3–0.5	0.97	32 ± 3	1 ± 1	44 ± 7	23 ± 6	0.52 ± 0.04	29.0 ± 1.0
	0.5–0.8	0.96	28 ± 3	6 ± 4	47 ± 8	19 ± 6	0.56 ± 0.03	21.7 ± 1.0
	0.8–1.4	0.95	25 ± 3	4 ± 2	30 ± 10	41 ± 6	0.53 ± 0.20	12.0 ± 1.1
2.0–2.2	0		24 ± 2 [a]	1 ± 1 [a]	58 ± 5 [a]	17 ± 6 [a]		42 [c]
	0.3–0.5	0.94	26 ± 5	8 ± 3	36 ± 4	30 ± 4	0.19 ± 0.08	18.8 ± 1.0
	0.5–0.8	0.93	16 ± 4	5 ± 2	34 ± 5	45 ± 4	0.40 ± 0.06	13.5 ± 1.0
	0.8–1.4	0.91	20 ± 8	1 ± 4	45 ± 6	34 ± 5	0.48 ± 0.09	11.2 ± 2.6
2.2–2.8	0		12 ± 1 [b]	2 ± 1 [b]	68 ± 4 [b]	18 ± 4 [b]		29 [c]
	0.3–0.5	0.86	10 ± 2	3 ± 2	52 ± 5	35 ± 4	0.20 ± 0.04	11.5 ± 0.6
	0.5–0.8	0.84	14 ± 5	2 ± 2	53 ± 4	31 ± 7	0.25 ± 0.07	8.8 ± 0.6
	0.8–1.4	0.81	16 ± 6	1 ± 2	29 ± 5	54 ± 8	0.45 ± 0.20	4.1 ± 0.6

[a] Results from ref. [11].
[b] Results from ref. [15].
[c] Results from ref. [12].
[d] These values were determined by refitting the data of ref. [11] with variable n.

4. The reaction $\gamma_V p \to \rho^0 p$

4.1. The rho mass shape

As described above the ρ mass shape was analyzed in terms of the skewing factor $(M_\rho/M_{\pi^+\pi^-})^n$ which has been found to give an adequate description of the mass distribution in photoproduction * [15]. For $|t| < 0.5$ GeV^2 and integrating over Q^2 our

* The form of the rho mass shape and the cross sections deduced from it are subject to theoretical uncertainty. Different approaches have been used in analyzing rho-photoproduction (see e.g. ref. [15]), e.g. the Söding model and the above parametrization. The resulting cross sections agreed to within 10–20% above W = 2 GeV. We use the above form because it provides the most convenient parametrization of the rho peak.

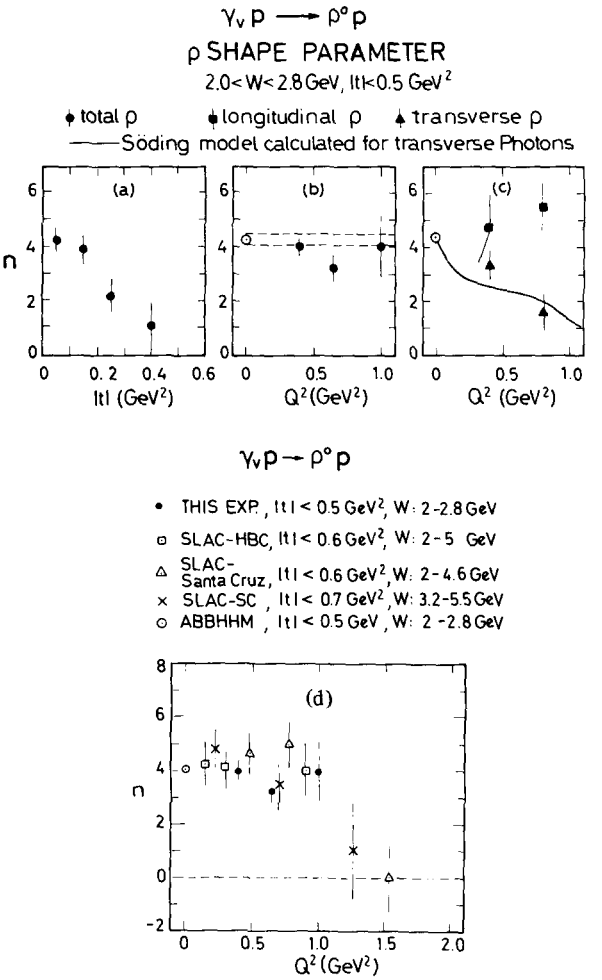

Fig. 6. Shape factor n of the ρ^0 for $2.0 < W < 2.8$ GeV and $|t| < 0.5$ GeV^2. The open circles are from a fit to the data of ref. [11]. (a) n *versus* $|t|$ for $0.3 < Q^2 < 1.4$ GeV^2. (b) n *versus* Q^2. (c) n *versus* Q^2 for longitudinal and transverse rhos separately. The full line is the prediction from the Söding model for transverse rhos. (d) n *versus* Q^2. Results from different experiments: •this experiment, ○ (ref. [11]), × (ref. [16]), □ (ref. [17]), △ (ref. [18]).

fit results were

$$\begin{aligned} n &= 6.0 \pm 0.2, \quad \text{for} \quad W = 1.7\text{–}2.0 \text{ GeV}, \\ &\quad 4.0 \pm 0.6, \qquad\qquad 2.0\text{–}2.2 \text{ GeV}, \\ &\quad 3.6 \pm 0.3, \qquad\qquad 2.2\text{–}2.8 \text{ GeV}^{\star}. \end{aligned}$$

* Fits without t cut gave $n = 5.2$ for $1.7 < W < 2$ GeV and $n = 4$ for $2.0 < W < 2.8$ GeV. These values were applied in the fits used for cross section determination (tables 2, 3, 4b, figs. 7, 8, 10, 11).

The large value of n in the first W interval is a consequence of a shoulder in the $M_{\pi^+\pi^-}$ distribution around 0.5 GeV (see fig. 4a) which is less prominent in the corresponding distribution in photoproduction (yielding $n = 4$).

We studied the t and Q^2 dependence (for $|t| < 0.5$ GeV^2) of n in the W interval 2.0–2.8 GeV. Fig. 6a shows n as a function of t. In close accord with photoproduction [15] the skewing is maximal near $t = 0$ ($n \simeq 4$–5) and appears to vanish around $|t| \simeq 0.5$ GeV^2. As shown in fig. 6b no statistically significant variation is observed with Q^2. The fitted n values are in agreement with the $Q^2 = 0$ result obtained from a fit we made to the data of ref. [11] in the same W bin. In fig. 6d we have compiled the results on the Q^2 dependence of n from previous experiments [15–18]. Clearly n is consistent with 4 for $Q^2 \lesssim 1$ GeV^2. For larger Q^2 there is an indication that n is decreasing.

We also have examined the mass shape of longitudinally and transversally polarized rhos separately by replacing the rho term in eq. (8) by three rho terms: the first multiplied by $W(\cos\theta_H) = \cos^2\theta_H$ (for longitudinal rhos); the second one with $W(\cos\theta) = \sin^2\theta_H(1 + \epsilon\cos 2\psi)$* (for transverse rhos), where ψ_H is the polarization angle in the helicity system defined below (subsect. 4.4.1); and thirdly a term with $n = 4$ (fixed) and $W(\cos\theta) = \text{const}$ (to describe unpolarized ρ's). The resulting n values are given in fig. 6c as a function of Q^2. While no significant Q^2 dependence is observed for longitudinal rhos, the amount of skewing decreases with Q^2 for the transverse part. The results are insensitive to the value of n assumed for the unpolarized rhos.

In photoproduction the rho shape can quantitatively be explained by the Söding model [19,15]; the skewing is caused by an interference of the rho amplitude with dipion production of the Drell type. We have extended the model for rho electroproduction and calculated the Q^2 dependence of n for transverse photons in this model. The resulting curve (see fig. 6c) describes the data points well. A similar evaluation for the longitudinal photon part is more difficult: due to the $\cos^2\theta_H$-like decay angular distribution a substantial fraction of the rho events have $p\pi^\pm$ masses in the resonance region ($M_{p\pi^\pm} \lesssim 1.5$ GeV). Therefore the full set of πN partial waves has to be taken into account when calculating the dipion terms. Such a calculation has not yet been done.

4.2. The ρ^0 cross section

The ρ^0 production cross section is shown in fig. 7 as a function of W for different

* This form projects out s-channel helicity conserving rhos produced *via* natural parity exchange (see the appendix).

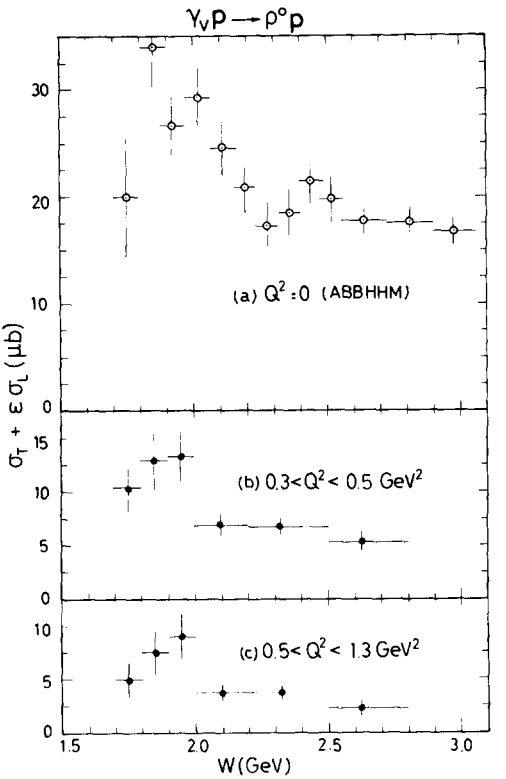

Fig. 7. $\sigma(\gamma_V p \to \rho^0 p)$ as a function of W for different Q^2 regions. The points at $Q^2 = 0$ for $W > 1.9$ GeV are results from ref. [11] using a ρ parametrization with $n = 4$. The open points for $W < 1.9$ GeV were obtained by us from a fit to the data of ref. [11] using a similar parametrization. (a) $Q^2 = 0$. (b) $0.3 < Q^2 < 0.5$ GeV^2. (c) $0.5 < Q^2 < 1.3$ GeV^2.

Q^2 intervals. A W dependence similar to photoproduction * (open points) is observed: σ_ρ rises sharply at threshold, goes through a maximum near $W = 1.9$ GeV and becomes nearly constant towards higher energies. The latter behaviour is suggestive of a diffractive mechanism. The Q^2 dependence of σ_ρ is given in fig. 8 and table 3 for different regions of W; the data show a rapid decrease of σ_ρ with increasing Q^2; e.g. at $Q^2 = 1$ GeV^2, σ_ρ is down by a factor of ~10 from the photoproduction value. For

* For a meaningful comparison it is mandatory to extract the ρ cross sections from photoproduction and electroproduction in a comparable way. Near threshold ($W \lesssim 2$ GeV) the magnitude of the ρ cross sections depends quite sensitively on the parametrization of the ρ peak. In order to obtain comparable results we refitted the photoproduction data of ref. [11] with our fitting procedure (eq. (8)) yielding $n = 4.1 \pm 1.0$ for $W = 1.7$–1.8 GeV and $n = 4.6 \pm 0.3$ for $W = 1.8$–1.9 GeV. For $W > 1.9$ GeV we use the cross sections of ref. [11] which were obtained from a fitting procedure similar to ours using $n = 4$ (fixed), $M_\rho = 778$ MeV and $\Gamma_\rho = 143$ MeV.

Table 3
Reaction $\gamma_V p \to \rho^0 p$, σ_ρ as a function of Q^2; for completeness we also give the total inelastic $\gamma_V p$ cross section $\sigma_{tot} = \sigma_T + \epsilon\sigma_L$ and the ratio σ_ρ/σ_{tot}. σ_{tot} was obtained by us from a fit to the single arm data of ref. [9]

W (GeV)	Q^2 (GeV^2)	σ_ρ (μb)	σ_{tot} (μb)	σ_ρ/σ_{tot}
1.7–2.0	0	27 ± 3 [a]	155	0.175 ± 0.020
	0.3–0.4	13.5 ± 1.4	110.9	0.122 ± 0.013
	0.4–0.5	11.6 ± 2.6	96.8	0.120 ± 0.027
	0.5–0.6	9.3 ± 1.2	91.1	0.102 ± 0.013
	0.6–0.8	11.3 ± 2.5	79.9	0.142 ± 0.031
	0.8–1.4	3.5 ± 1.3	57.9	0.060 ± 0.022
2.0–2.2	0	25 ± 2 [a]	146	0.171 ± 0.014
	0.3–0.4	9.8 ± 1.6	93.5	0.105 ± 0.017
	0.4–0.5	4.3 ± 1.1	84.9	0.051 ± 0.013
	0.5–0.6	5.2 ± 1.5	77.6	0.067 ± 0.019
	0.6–0.8	4.2 ± 1.0	68.1	0.062 ± 0.015
	0.8–1.4	5.1 ± 1.7	51.8	0.098 ± 0.033
2.2–2.8	0	18.5 ± 1.5 [a]	135	0.137 ± 0.011
	0.3–0.4	6.0 ± 1.0	82.5	0.073 ± 0.012
	0.4–0.5	5.9 ± 1.0	73.7	0.080 ± 0.014
	0.5–0.6	3.9 ± 0.7	67.0	0.058 ± 0.010
	0.6–0.8	5.4 ± 1.1	58.7	0.092 ± 0.019
	0.8–1.4	1.2 ± 0.3	44.4	0.027 ± 0.007

[a] Obtained from the data of ref. [11] as described in caption of fig. 7.

comparison we show in fig. 8 the cross sections of refs. [18] and [20] *, which are compatible with our data.

4.3. Rho production angular distribution

The differential cross sections $d\sigma/d\Omega_{c.m.s.}$ and $d\sigma/dt$ were determined by separate Dalitz plot fits for each interval of $\cos\theta_{c.m.s.}$ and t (here $\theta_{c.m.s.}$ is the production angle in the $\gamma_V p$ c.m. system) **. The results are given in figs. 9, 10 and in table 4 for different $W - Q^2$ intervals. The use of $d\sigma/d\Omega_{c.m.s.}$ is advantageous in the low W region where the minimum momentum transfer varies rapidly accross the $W-Q^2$ interval.

We first discuss the low W region ($W < 2$ GeV). Here the angular distribution

* Ahrens et al. have measured the sum of the ρ^0 and ω cross sections. In order to deduce from these data the ρ^0 cross sections we used our data on ω production (ref. [3]) and subtracted the ω contribution.

** Separate fits in the threshold region (1.7–2 GeV) indicated a moderate dependence of the mass skewing parameter n on $\cos\theta_{c.m.s.}$ ($n = 5.8$ for $\cos\theta_{c.m.s.} > 0.6$, $n = 5.2$ for $-0.2 < \cos\theta_{c.m.s.} < 0.6$ and $n = 4$ for $\cos\theta_{c.m.s.} < -0.2$). These values were used for the electroproduction results in fig. 9. For $W > 2$ GeV the fitted ρ fractions were insensitive to the value of n. Here, $n = 4$ was used.

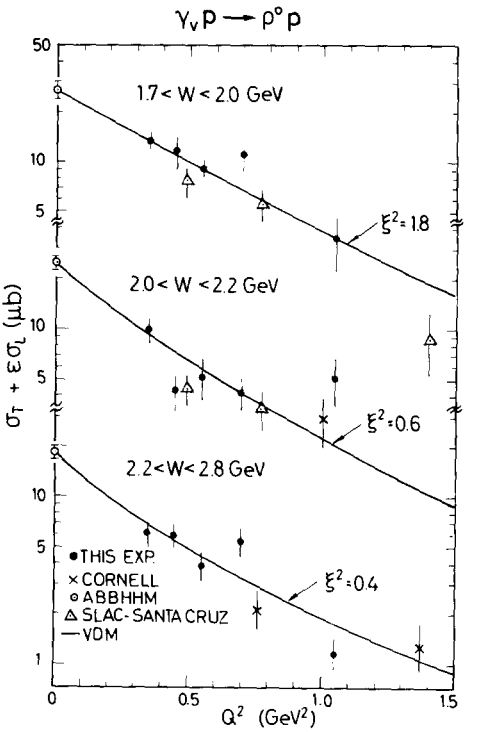

Fig. 8. $\sigma(\gamma_V p \rightarrow \rho^0 p)$ as a function of Q^2 for different W regions. The curves are a prediction of the vector dominance model (see subsect. 4.5). The points labelled SLAC-Santa Cruz and Cornell are from refs. [18] and [20], respectively. The open points, labelled ABBHHM, are data from ref. [11] as given in fig. 7.

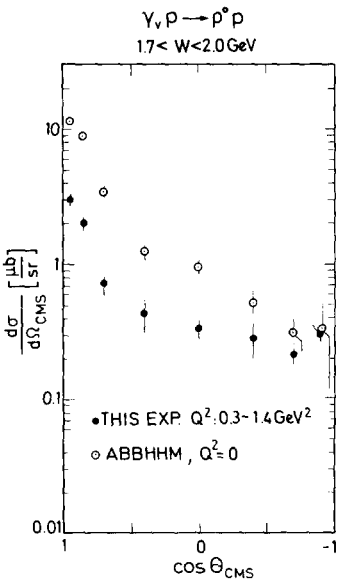

Fig. 9. $d\sigma/d\Omega_{c.m.s.}$ for $1.7 < W < 2.0$ GeV and $0.3 < Q^2 < 1.4$ GeV^2. The values of the shape parameter n used are given in the footnote to subsect. 4.3. The open points at $Q^2 = 0$ were obtained by refitting the data of ref. [11] with eq. (8) (the parameters used were $M_\rho = 780$ MeV, $\Gamma_\rho = 150$ MeV, $n = 4.8$ for $0.6 < \cos\theta_{c.m.s.} < 1.0$, $n = 0$ for $\cos\theta_{c.m.s.} < 0.6$).

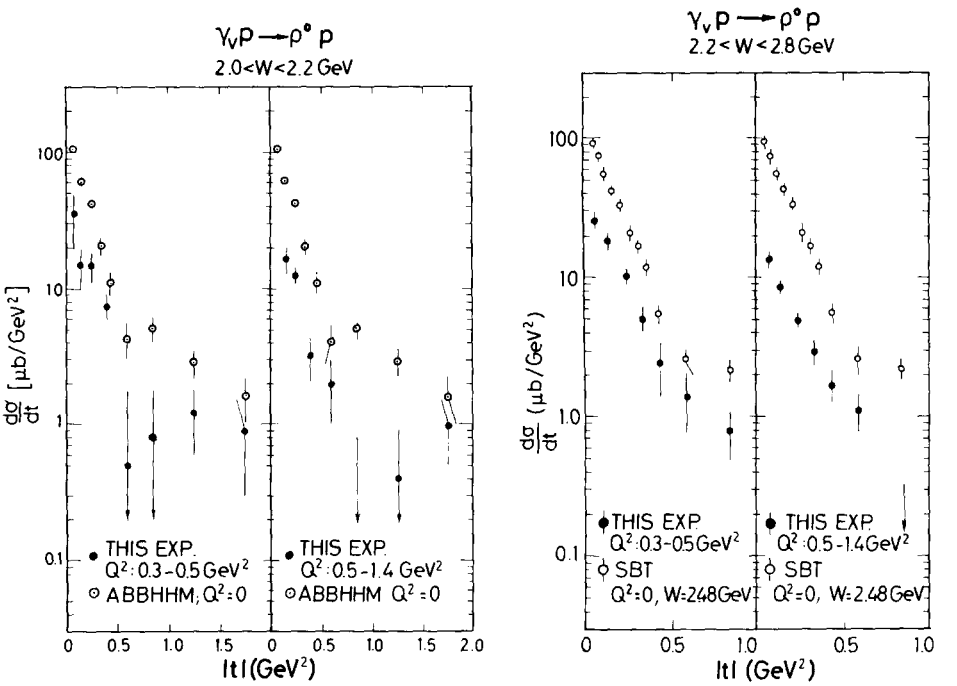

Fig. 10. $d\sigma/dt$ ($\gamma_V p \to \rho^0 p$) for different W and Q^2 regions. The open points labelled ABBHHM were obtained by refitting the data of ref. [11] in the appropriate intervals. The points labelled SBT are from table 12 of ref. [15] (parametrization cross section).

$d\sigma/d\Omega_{c.m.s.}$ has two components: a forward peaked (peripheral) part which decreases in magnitude with increasing Q^2, and a practically isotropic part (s-wave like) whose magnitude depends only weakly on Q^2 (see fig. 9). The two components have different W dependences. To show this we have determined the total cross section of the two components as follows: for the non-peripheral part the rho cross section was taken in the region $\cos\theta_{c.m.s.} < 0$, which is free of peripheral contributions, and was integrated over the full $\cos\theta_{c.m.s.}$ range assuming a symmetrical behaviour around $\cos\theta_{c.m.s.} = 0$. This leads to $\sigma_\rho^{\text{non-peripheral}}$. The peripheral component is then $\sigma_\rho^{\text{peripheral}} = \sigma_\rho - \sigma_\rho^{\text{non-peripheral}}$. The W dependence of the two components is shown in fig. 11. Both cross sections rise steeply near threshold; the peripheral part becomes nearly constant above $W = 2.0$ GeV while the non-peripheral contribution falls off rapidly above $W = 2.0$ GeV. This behaviour could be due to contributions from s-channel resonances. The almost isotropic angular distribution in the backward hemisphere (for $W < 2$ GeV) suggests an $L = 0$, $J^P = \frac{1}{2}^-$ or $\frac{3}{2}^-$ assignment for the $\rho^0 p$ system.

At energies above $W = 2$ GeV the peripheral component is dominant and the differential cross section is of the form (see fig. 10)

$$d\sigma/dt \sim \exp(At).$$

Table 4a
Reaction $\gamma_V p \to \rho^0 p$; differential cross section $d\sigma/d\Omega_{c.m.s.}$ (μb/sr) as obtained from maximum likelihood fits in $\cos\theta_{c.m.s.}$ intervals for $1.7 < W < 2.0$ GeV

$\cos\theta_{c.m.s.}$ \ Q^2 (GeV^2)	0 [a]	0.3–1.4 $\langle Q^2 \rangle = 0.7$ GeV^2
0.9–1.0	11.5 ± 0.6	3.0 ± 0.3
0.8–0.9	7.8 ± 0.7	2.0 ± 0.24
0.6–0.8	3.4 ± 0.3	0.72 ± 0.13
0.2–0.6	1.25 ± 0.16	0.43 ± 0.12
(−0.2)–0.2	0.96 ± 0.10	0.33 ± 0.06
(−0.6)–(−0.2)	0.52 ± 0.11	0.28 ± 0.08
(−0.8)–(−0.6)	0.31 ± 0.08	0.22 ± 0.04
(−1.0)–(−0.8)	0.32 ± 0.20	0.31 ± 0.05

[a] Obtained by fitting the data of ref. [11] (see caption of fig. 9).

Table 4b
Reaction $\gamma_V p \to \rho^0 p$; differential cross section $d\sigma/dt$ (μb/GeV^2) for $2.0 < W < 2.2$ GeV ($\langle W \rangle = 2.09$ GeV) and $2.2 < W < 2.8$ GeV ($\langle W \rangle = 2.45$ GeV) (for numerical values at $Q^2 = 0$ and $\langle W \rangle = 2.48$ GeV, see table 12 of ref. [15])

	$2.0 < W < 2.2$ GeV			$2.2 < W < 2.8$ GeV	
$\lvert t\rvert$ (GeV^2) \ Q^2 (GeV^2)	0 [a]	0.3–0.5 $\langle Q^2 \rangle = 0.4$	0.5–1.4 $\langle Q^2 \rangle = 0.95$	0.3–0.5 $\langle Q^2 \rangle = 0.42$	0.5–1.4 $\langle Q^2 \rangle = 0.85$
$\lvert t\rvert_{min}$–0.1 [a]	105 ± 10	35 ± 15		27.0 ± 3.1	13.5 ± 1.9
0.1–0.2	62 ± 4.5	15 ± 5	16.7 ± 3.9 [b]	18.0 ± 2.0	8.6 ± 0.9
0.2–0.3	42.5 ± 3.0	14.4 ± 3.5	12.6 ± 2.0	10.2 ± 1.3	5.0 ± 0.7
0.3–0.4	20.4 ± 3.1	7.5 ± 1.6	3.2 ± 1.1	5.2 ± 1.0	2.9 ± 0.6
0.4–0.5	11.2 ± 2.2			2.4 ± 1.0	1.7 ± 0.5
0.5–0.7	4.1 ± 1.3	0.5 ± 1.3	2.0 ± 1.0	1.4 ± 0.6	1.1 ± 0.3
0.7–1.0	5.1 ± 1.0	0.8 ± 1.0	0 ± 0.8	0.8 ± 0.3	0.03 ± 0.15
1.0–1.5	2.9 ± 0.7	1.2 ± 0.6	0.4 ± 0.5	0 ± 0.22	0.20 ± 0.12
1.5–2.0	1.6 ± 0.6	0.9 ± 0.6	1.0 ± 0.5	0 ± 0.14	0.07 ± 0.07
$\lvert t\rvert_{min}$ (GeV^2)	0.025	0.075	0.13	0.04	0.06

[a] Obtained by fitting the data of ref. [11] in the appropriate intervals (with shape parameter $n = 4$).
[b] For $\lvert t\rvert$ interval 0.13–0.2 GeV^2.

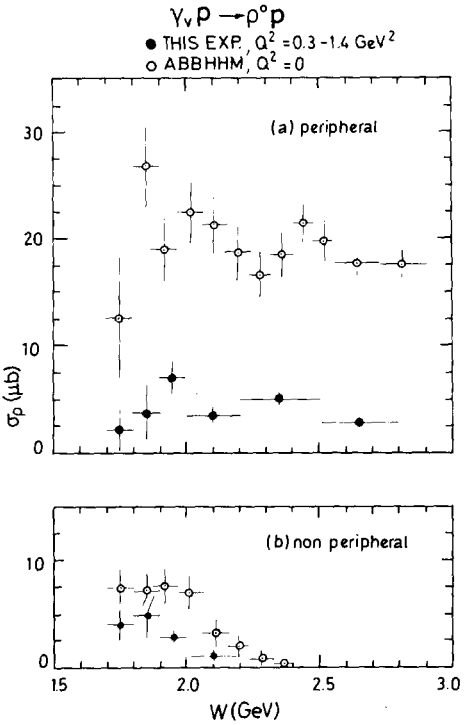

Fig. 11. $\sigma(\gamma_V p \to \rho^0 p)$ as a function of W for (a) peripheral and (b) non-peripheral contributions (see subsect. 4.3). The open points were obtained from fits to the data of ref. [11].

Fits to $d\sigma/dt$ in the W interval 2.2–2.8 GeV and for $0.1 < |t| < 0.5$ GeV^2 yielded the following slope values

$$A = 6.5 \pm 0.5 \text{ GeV}^{-2} \quad \text{for} \quad Q^2 = 0.3 - 0.5 \text{ GeV}^2,$$
$$5.7 \pm 0.7 \text{ GeV}^{-2} \quad \text{for} \quad Q^2 = 0.5 - 1.4 \text{ GeV}^2.$$

The slope parameter was also determined from a Dalitz plot fit in which the rho term in eq. (8) was multiplied by $\exp At$. The resulting A values are shown in fig. 12a together with the value fitted at $Q^2 = 0$, namely $A = 6.5 \pm 0.3$ GeV^{-2}. The data are consistent with no change of the rho slope with increasing Q^2.

In an optical model the slope A measures the interaction radius of photon and proton, $A_{\rho p} \simeq \frac{1}{4}(R_\gamma^2 + R_p^2)$. It has been argued that with increasing Q^2 the radius of the photon will shrink [21]. Maximal shrinkage ($R_\gamma = 0$) would lead to $A_{\rho p} \simeq \frac{1}{2}A_{pp}$ ($\simeq$3.5 GeV^{-2} at $W \approx 3$ GeV), where A_{pp} is the slope for elastic pp scattering. Hence maximal shrinkage is excluded by our data for $W \simeq 2.5$ GeV and $Q^2 \lesssim 1$ GeV^2.

In addition we determined the slope parameter A for longitudinally and transversely polarized rhos separately. This was done as follows: The probability for each event to be due to ρ production is equal to the weight factor $W_\rho^i \propto a_\rho F_\rho(M^i_{\pi^+\pi^-})$

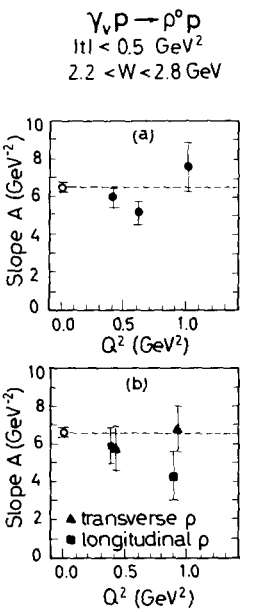

Fig. 12. (a) Reaction $\gamma_V p \to \rho^0 p$. Slope of $d\sigma/dt$ for $2.2 < W < 2.8$ GeV and $|t| < 0.5$ GeV^2 as a function of Q^2. (b) The same as (a), but for transverse and longitudinal rhos separately. The open points are from a fit to the data of ref. [11].

determined in the maximum likelihood fit to the Dalitz plot (eq. (8)). The weight factor W_ρ^i multiplied by $\cos^2\theta_H$ projects out longitudinal rho events; similarly, multiplication by $\sin^2\theta_H(1 + \epsilon \cos 2\psi_H)$ projects out transverse rho mesons. The t dependence of these two parts was fitted separately and the result is plotted in fig. 12b. No statistically significant difference between the slopes of longitudinal and transverse rhos is observed.

4.4. Rho decay angular distributions

4.4.1. Introduction. The ρ decay acts as an analyzer of the spin states of the rho. Hence an analysis of the rho decay distribution allows us to study the spin-dependent properties of the production process. The relevant formalism has been developed in ref. [14]. We present in the appendix a summary of the formulae applicable to our work. In the following we restrict ourselves to (a) defining the angles used for the decay analysis and (b) quoting the decay distribution for the (simplified) case of s-channel helicity conservation. Results will be given and discussed in subsect. 4.4.2.

The rho decay was studied in the s-channel helicity system, which is the most convenient system for describing the rho decay from photoproduction [15]. The ρ direction in the overall hadron c.m.s. is taken as the quantization axis. The pions from ρ decay are described by the polar angle θ_H and the azimuthal angle ϕ_H in the $\pi^+\pi^-$ rest

system (see the appendix for a formal definition). We also use the angle Φ of the polarization vector of the transverse photons in the hadron c.m.s., which is given by the angle between the ρ production plane and the electron scattering plane.

We analyzed the ρ^0 decay angular distribution $W(\cos\theta_H, \phi_H, \Phi)$ in terms of the ρ^0 density matrix in the helicity system using the formalism of ref. [14]. The ρ^0 density matrix, ρ_{ik}, in general, can be decomposed into six independent matrices ρ^α_{ik}, where the matrices for $\alpha = 0$–2 and 4 describe ρ^0 production by transverse and longitudinal photons, respectively; the matrices for $\alpha = 5$–6 measure transverse/longitudinal interference terms. When, as in this experiment, the ratio of the longitudinal to transverse photon flux as measured by ϵ is not varied, the contributions from ρ^0 and ρ^4 cannot be separated and $W(\cos\theta_H, \phi_H, \Phi)$ measures certain combinations of the ρ^α_{ik}:

$$r^{04}_{ik} = \frac{\rho^0_{ik} + \epsilon R \rho^4_{ik}}{1 + \epsilon R} , \tag{12a}$$

$$r^\alpha_{ik} = \frac{\rho^\alpha_{ik}}{1 + \epsilon R} , \qquad \alpha = 1\text{–}2 , \tag{12b}$$

$$r^\alpha_{ik} = \frac{\sqrt{R}\,\rho^\alpha_{ik}}{1 + \epsilon R} , \qquad \alpha = 5\text{–}6 , \tag{12c}$$

where $R = \sigma_L/\sigma_T$ is the ratio of the cross sections for ρ^0 production by longitudinal and transverse photons. Note that as $Q^2 \to 0$, $r^{04}_{ik} \to \rho^0_{ik}$ and $r^\alpha_{ik} \to \rho^\alpha_{ik}$ ($\alpha = 1$–2). The full decay distribution, expressed in terms of the 15 measurable matrix elements, is given in the appendix.

If the s-channel helicity is conserved (SCHC) at the $\gamma\rho$ vertex all matrix elements except r^{04}_{00}, $r^1_{1\text{-}1}$, Im $r^2_{1\text{-}1}$, Re r^5_{10}, Im r^6_{10} are zero. Furthermore $r^1_{1\text{-}1} = -\text{Im}\, r^2_{1\text{-}1}$ and Re $r^5_{10} = -\text{Im}\, r^6_{10}$. In this case the decay distribution reduces to

$$W(\cos\theta_H, \psi_H) = \frac{3}{4\pi}\left[\tfrac{1}{2}(1 - r^{04}_{00}) + \tfrac{1}{2}(3r^{04}_{00} - 1)\cos^2\theta_H + \epsilon r^1_{1\text{-}1}\sin^2\theta_H \cos 2\psi_H - 2\sqrt{\epsilon(1+\epsilon)}\,\text{Re}\, r^5_{10} \sin 2\theta_H \cos\psi_H\right] . \tag{13}$$

Here we used the polarization angle $\psi_H = \phi_H - \Phi$. The term $\sin^2\theta_H \cos 2\psi_H$ characterises transverse rhos while contributions from longitudinal rhos have a $\cos^2\theta_H$ distribution and no ψ_H dependence. The last term is due to longitudinal-transverse interference.

4.4.2. Results. In this subsection we give the experimental results on the decay distributions and density matrix elements and discuss the related properties of the production process *.

* In the present experiment we analyse the decay distribution by averaging over the rho mass distribution. In the SBT photoproduction experiment [15] it was possible to measure the variation of the decay properties as a function of $M_{\pi^+\pi^-}$. This is statistically impossible in our experiment.

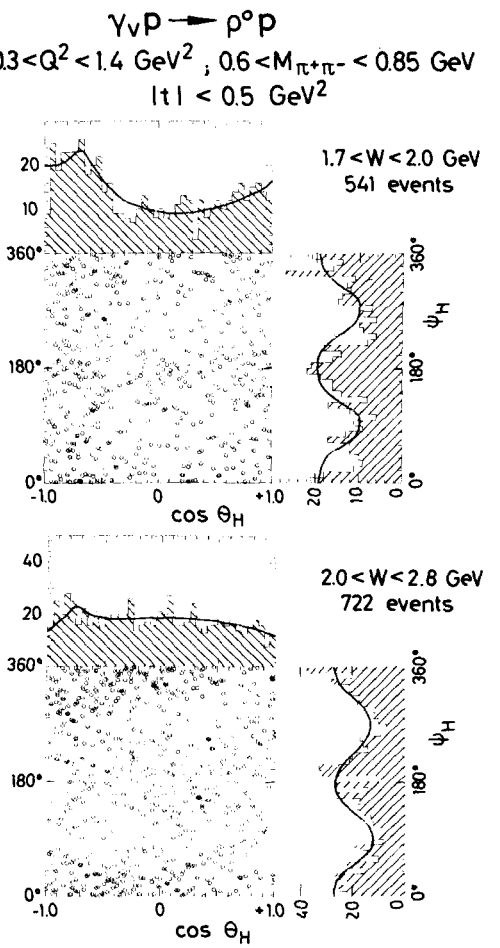

Fig. 13. Decay angular distributions for $\gamma_V p \to \pi^+\pi^- p$ in the ρ region ($0.6 < M_{\pi^+\pi^-} < 0.85$ GeV) for $|t| < 0.5$ GeV^2, $0.3 < Q^2 < 1{:}4$ GeV^2 in the energy intervals $1.7 < W < 2.0$ GeV and $2.0 < W < 2.8$ GeV. The curves are from a maximum likelihood fit.

Fig. 13 shows scatter plots of $\cos\theta_H$ *versus* the polarization angle $\psi_H = \phi_H - \Phi$ for events in the mass region of the rho and small $|t|$ ($|t| < 0.5$ GeV^2). The curves drawn in the projections show the result from the maximum likelihood fits (eq. (8)). We see from $W(\cos\theta_H)$ (fig. 13) that at low energies ($W < 2$ GeV) production of longitudinal rhos dominates. The broad bump in the $\cos\theta_H$ spectrum near $\cos\theta_H = -1$ is a reflection of Δ^{++} production. Above $W = 2$ GeV the shape of $W(\cos\theta_H)$ has changed to a more $\sin^2\theta$ like distribution. Consequently, more transverse than longitudinal rhos are being produced at higher W. The non-uniformity of the ψ_H distribution demonstrates the presence of contributions from transverse photons in both

Table 5
Spin-density matrix elements for $\gamma_V p \to \rho^0 p$ in the s-channel helicity system ($|t| < 0.5$ GeV^2, $0.3 < Q^2 < 1.4$ GeV^2)

W (GeV)	1.7–1.8	1.8–1.9	1.9–2.0	2.0–2.2	2.2–2.4	2.4–2.8
r^{04}_{00}	0.69 ± 0.05	0.69 ± 0.05	0.56 ± 0.05	0.33 ± 0.04	0.22 ± 0.04	0.20 ± 0.04
Re r^{04}_{10}	0.07 ± 0.03	0.13 ± 0.03	0.12 ± 0.03	0.08 ± 0.02	0.08 ± 0.03	0.09 ± 0.03
r^{04}_{1-1}	−0.01 ± 0.03	−0.04 ± 0.03	−0.11 ± 0.04	−0.01 ± 0.03	−0.09 ± 0.04	0.04 ± 0.04
r^{1}_{00}	0.22 ± 0.09	−0.12 ± 0.09	−0.15 ± 0.09	0.16 ± 0.07	0.00 ± 0.07	0.05 ± 0.07
r^{1}_{11}	−0.02 ± 0.04	0.03 ± 0.04	−0.03 ± 0.04	−0.09 ± 0.04	−0.12 ± 0.05	0.02 ± 0.05
Re r^{1}_{10}	0.00 ± 0.05	0.00 ± 0.04	−0.11 ± 0.05	−0.07 ± 0.04	0.02 ± 0.04	0.05 ± 0.04
r^{1}_{1-1}	0.07 ± 0.05	0.16 ± 0.05	0.17 ± 0.06	0.16 ± 0.05	0.29 ± 0.06	0.40 ± 0.07
Im r^{2}_{10}	−0.07 ± 0.05	0.03 ± 0.04	0.03 ± 0.04	0.02 ± 0.04	0.02 ± 0.04	0.03 ± 0.04
Im r^{2}_{1-1}	−0.04 ± 0.05	−0.13 ± 0.05	−0.13 ± 0.06	−0.17 ± 0.06	−0.29 ± 0.06	−0.36 ± 0.07
r^{5}_{00}	−0.03 ± 0.04	−0.01 ± 0.05	0.07 ± 0.05	0.04 ± 0.03	−0.01 ± 0.04	0.01 ± 0.03
r^{5}_{11}	0.01 ± 0.02	0.02 ± 0.02	0.02 ± 0.02	−0.01 ± 0.02	0.04 ± 0.03	0.00 ± 0.03
Re r^{5}_{10}	−0.02 ± 0.02	0.02 ± 0.02	0.02 ± 0.03	0.00 ± 0.02	0.07 ± 0.02	0.10 ± 0.02
r^{5}_{1-1}	−0.04 ± 0.02	−0.02 ± 0.02	−0.04 ± 0.03	0.00 ± 0.02	−0.07 ± 0.03	−0.03 ± 0.03
Im r^{6}_{10}	−0.02 ± 0.02	−0.02 ± 0.02	−0.04 ± 0.02	−0.06 ± 0.02	−0.07 ± 0.02	−0.09 ± 0.02
Im r^{6}_{1-1}	0.07 ± 0.02	0.02 ± 0.02	0.04 ± 0.03	0.02 ± 0.03	0.09 ± 0.03	0.07 ± 0.03

Table 6
Spin density matrix elements for $\gamma_V p \to \rho^0 p$ in the s-channel helicity system ($|t| < 0.5$ GeV^2, $1.7 < W < 2.0$ GeV and $2.0 < W < 2.8$ GeV)

	$\langle Q^2 \rangle$ (GeV^2)	W (GeV)	
		1.7–2.0	2.0–2.8
r^{04}_{00}	0.0	0.33 ± 0.02 [a]	0.04 ± 0.01 [a]
	0.4	0.60 ± 0.03	0.20 ± 0.03
	0.65	0.69 ± 0.05	0.28 ± 0.04
	1.05	0.97 ± 0.12	0.47 ± 0.08
Re r^{04}_{10}	0.0	0.05 ± 0.01 [a]	0.01 ± 0.01 [a]
	0.4	0.09 ± 0.02	0.08 ± 0.02
	0.65	0.14 ± 0.03	0.08 ± 0.03
	1.05	0.14 ± 0.08	0.16 ± 0.06
r^{04}_{1-1}	0.0	−0.02 ± 0.01 [a]	−0.02 ± 0.01 [a]
	0.4	−0.05 ± 0.03	−0.02 ± 0.03
	0.65	−0.07 ± 0.03	−0.00 ± 0.04
	1.05	0.04 ± 0.06	−0.06 ± 0.07
r^{1}_{00}	0.4	−0.02 ± 0.06	−0.01 ± 0.05
	0.65	0.01 ± 0.10	0.15 ± 0.07
	1.05	−0.18 ± 0.32	0.26 ± 0.13
r^{1}_{11}	0.4	0.01 ± 0.03	−0.05 ± 0.04
	0.65	−0.04 ± 0.04	−0.05 ± 0.05
	1.05	0.07 ± 0.09	−0.16 ± 0.08
Re r^{1}_{10}	0.4	0.02 ± 0.03	−0.02 ± 0.03
	0.65	−0.17 ± 0.05	0.02 ± 0.04
	1.05	0.03 ± 0.13	0.07 ± 0.09
r^{1}_{1-1}	0.4	0.13 ± 0.04	0.31 ± 0.05
	0.65	0.18 ± 0.05	0.33 ± 0.06
	1.05	−0.16 ± 0.09	0.00 ± 0.12
Im r^{2}_{10}	0.4	−0.01 ± 0.03	0.01 ± 0.03
	0.65	0.00 ± 0.05	0.06 ± 0.04
	1.05	0.09 ± 0.10	−0.01 ± 0.08
Im r^{2}_{1-1}	0.4	−0.12 ± 0.04	−0.33 ± 0.05
	0.65	−0.06 ± 0.05	−0.21 ± 0.06
	1.05	−0.05 ± 0.11	−0.17 ± 0.12
r^{5}_{00}	0.4	−0.02 ± 0.03	0.00 ± 0.03
	0.65	0.07 ± 0.05	0.04 ± 0.03
	1.05	−0.12 ± 0.15	−0.04 ± 0.07
r^{5}_{1-1}	0.4	−0.03 ± 0.02	−0.03 ± 0.02
	0.65	−0.05 ± 0.03	−0.04 ± 0.03
	1.05	0.03 ± 0.03	−0.04 ± 0.05
Re r^{5}_{10}	0.4	−0.01 ± 0.02	0.07 ± 0.02
	0.65	0.05 ± 0.03	0.07 ± 0.02
	1.05	−0.05 ± 0.05	−0.06 ± 0.04

Table 6 (continued)

	$\langle Q^2 \rangle$ (GeV^2)	W (GeV) 1.7–2.0	W (GeV) 2.0–2.8
r^5_{11}	0.4	0.02 ± 0.01	0.02 ± 0.02
	0.65	0.02 ± 0.02	0.00 ± 0.02
	1.05	0.01 ± 0.05	0.00 ± 0.04
Im r^6_{10}	0.4	−0.04 ± 0.02	−0.07 ± 0.01
	0.65	−0.02 ± 0.02	−0.07 ± 0.02
	1.05	0.01 ± 0.06	−0.08 ± 0.04
Im r^6_{1-1}	0.4	0.03 ± 0.02	0.06 ± 0.02
	0.65	0.06 ± 0.02	0.06 ± 0.03
	1.05	0.07 ± 0.06	0.09 ± 0.05

a) Obtained by fitting the photoproduction data of ref. [11].

energy regions. The decay pions cluster near $\psi_H = 0°$ and 180° which is evidence for dominant natural parity exchange in the s-channel helicity conserving part (see below).

The density matrix elements were determined by the method of moments weighting each event with the maximum likelihood weight factor $W^i_\rho \propto a_\rho F_\rho(M^i_{\pi^+\pi^-})$. By this weighting procedure the contamination by background is minimized ★. The 15 independent density matrix elements measurable in this experiment are shown in fig. 14 as a function of W and in fig. 15 as a function of Q^2. They are also listed in tables 5 and 6. The dash-dotted lines in figs. 14 and 15 give the behaviour expected for s-channel helicity conservation. The open points in the top parts of figs. 14 and 15 give the related matrix elements ρ^0_{00}, Re ρ^0_{10} and ρ^0_{1-1} from the photoproduction data of ref. [11]. We find

★ We have estimated the contamination by background in the following way: (a) $W > 2$ GeV. Events with $M_{\pi^+\pi^-} > 1$ GeV where the contribution of rho is negligible, have a flat angular distribution in ϕ_H and Φ. Hence assuming that the background under the rho has the same characteristics, the rho density matrix elements that depend on ϕ_H and Φ will not be influenced by this background. We have also determined r^{04}_{00} (which depends on θ_H only) from a Dalitz plot fit in which background due to Δ^{++} and phase space is taken into account; we find values which agree within one standard deviation with those from the moments analysis, indicating the range of systematic uncertainty of r^{04}_{00} for $W > 2$ GeV. (b) $W < 2$ GeV. Here the background peaks under the rho and is cut off by kinematics at 1 GeV (fig. 4a). The r_{ik} determined from the weighted moments method give a consistent description of the ψ_H distribution assuming an isotropic background in ϕ_H and Φ. This gives confidence in the values of the elements depending on ϕ_H and Φ (all but r^{04}_{00}). The element r^{04}_{00}, on the other hand, is very sensitive to the fitted shape of the rho. From a comparison of different fits we conclude that the systematic uncertainty of r^{04}_{00} is of the order of 0.1 and 0.2 for $0.3 < Q^2 < 0.8$ and $0.8 < Q^2 < 1.4$ GeV^2, respectively, for $W < 2$ GeV.

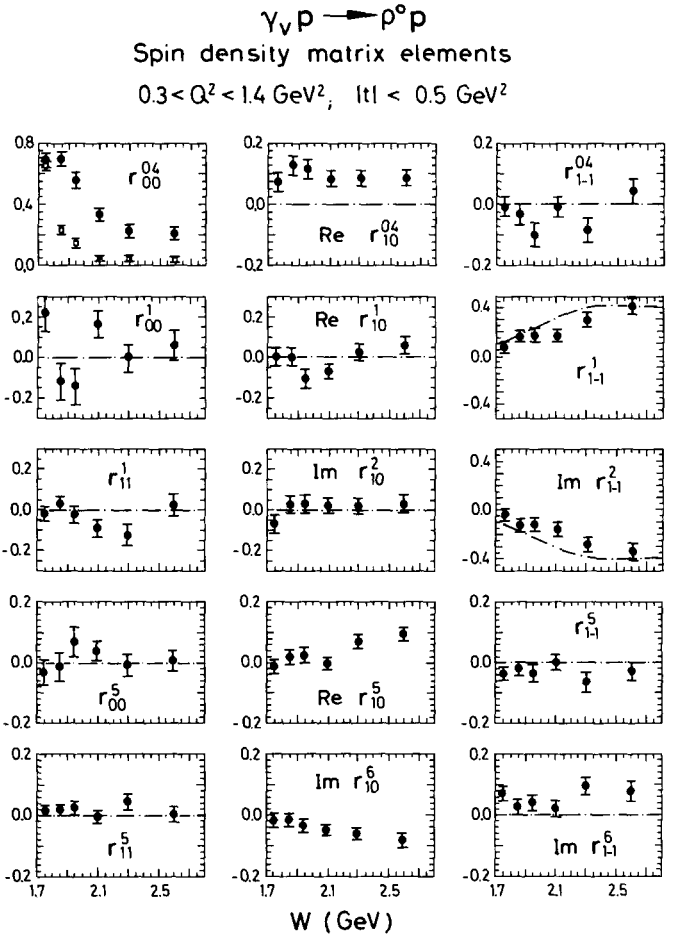

Fig. 14. Reaction $\gamma_V p \rightarrow \rho^0 p$. Density matrix elements for the ρ^0 as a function of W in the region $0.3 < Q^2 < 1.4$ GeV^2 and $|t| < 0.5$ GeV^2. The dash-dotted lines give the behaviour expected from s-channel helicity conservation. The curves for r^1_{1-1} and Im r^2_{1-1} assume in addition natural parity exchange only. The open points (at $Q^2 = 0$) were obtained by us by fitting the photoproduction data of ref. [11].

(a) a strong variation of r^{04}_{00} and ρ^0_{00} with W. At threshold r^{04}_{00} and ρ^0_{00} are of the order of 0.7, i.e. in both photo- and electroproduction more longitudinal than transverse rhos are being produced. This implies strong helicity flip contributions in rho-photoproduction. With increasing W the fraction of longitudinal rhos drops rapidly. In photoproduction ρ^0_{00} is close to zero for $W > 2$ GeV; in electroproduction r^{04}_{00} approaches a constant value of 0.2 to 0.3.

(b) a linear rise of r^{04}_{00} with Q^2 corresponding to an increase in the ratio of longitudinal to transverse rhos with Q^2.

(c) an increase of r^1_{1-1} and $|\mathrm{Im}\, r^2_{1-1}|$ with W. These elements determine the anisotropy of the ψ distribution (see eq. (13)).

(d) a slow rise of $\mathrm{Re}\, r^5_{10}$ and $|\mathrm{Im}\, r^6_{10}|$ with W which indicates increasing interference between the rho production amplitudes by longitudinal and transverse photons (see eq. (13)).

(e) that except for $\mathrm{Re}\, r^{04}_{10}$ and possibly $\mathrm{Im}\, r^6_{1-1}$ all other matrix elements are consistent with SCHC. This leads to the conclusion that electroproduction of rho mesons approximately obeys SCHC. Elements like $\mathrm{Re}\, r^{04}_{10}$ are particularly sensitive to helicity flip contributions since they depend on the interference of flip with non-flip amplitudes.

From the values of the r_{ik} we can make the following quantitative determinations:

(i) Natural parity exchange cross section

From the values of r^1_{00} and r^1_{1-1} we can deduce a lower limit for $\sigma^{\mathrm{N}}_{\mathrm{T}}$, the contribution of natural parity exchange in the t-channel to rho production by transverse photons (see subsect. 4.2 of ref. [14]):

$$\sigma^{\mathrm{N}}_{\mathrm{T}} \geqslant \tfrac{1}{2}\{1 + (2r^1_{1-1} - r^1_{00})\}\,\sigma_{\mathrm{T}} \,. \tag{14}$$

The result is that $\sigma^{\mathrm{N}}_{\mathrm{T}} \geqslant (0.83 \pm 0.06)\sigma_{\mathrm{T}}$ for $2.2 < W < 2.8$ GeV and $0.3 < Q^2 < 1.4$ GeV^2. Thus rho production by transverse photons proceeds primarily through natural parity exchange as expected for a diffractive process.

(ii) s-channel helicity conservation

We estimate the size of helicity single flip contributions from the value of $\mathrm{Re}\, r^{04}_{10}$. The expression of $\mathrm{Re}\, r^{04}_{10}$ in terms of helicity amplitudes T is given in the appendix. With the assumption that the ratio of helicity single-flip to helicity non-flip contributions is the same for longitudinal and transverse photons we obtain the approximate expression

$$\frac{|T_{\mathrm{flip}}|}{|T_{\mathrm{non\text{-}flip}}|} = \mathrm{Re}\, r^{04}_{10}\, \frac{2(1+\epsilon R)}{1+2\epsilon R} \,. \tag{15}$$

Inserting the measured values of $\mathrm{Re}\, r^{04}_{10}$ (table 6) and R (table 7) for $2.1 < W < 2.8$ GeV and $|t| < 0.5$ GeV^2 we obtain

$$\frac{|T_{\mathrm{flip}}|}{|T_{\mathrm{non\text{-}flip}}|} = \begin{matrix} 0.14 \pm 0.04 \\ 0.13 \pm 0.04 \\ 0.22 \pm 0.09 \end{matrix} \quad \text{for} \quad \begin{matrix} 0.3\text{–}0.5\ \mathrm{GeV}^2 \\ Q = 0.5\text{–}0.8\ \mathrm{GeV}^2 \\ 0.8\text{–}1.4\ \mathrm{GeV}^2 \end{matrix}$$

Hence with the above assumption the helicity single-flip amplitudes are of the order of 15–20% of the non-flip amplitudes for $|t| < 0.5$ GeV^2. In photoproduction at $W = 2.48$ GeV the amplitude ratio $|T_{01}|/|T_{11}| \simeq 2\ \mathrm{Re}\, \rho^0_{10}$ was found to be 0.04 ± 0.02 for $|t| < 0.4$ GeV^2 [15]. (The $T_{\lambda_\rho \lambda_\gamma}$ are helicity amplitudes for rho and photon helicities λ_ρ and λ_γ.)

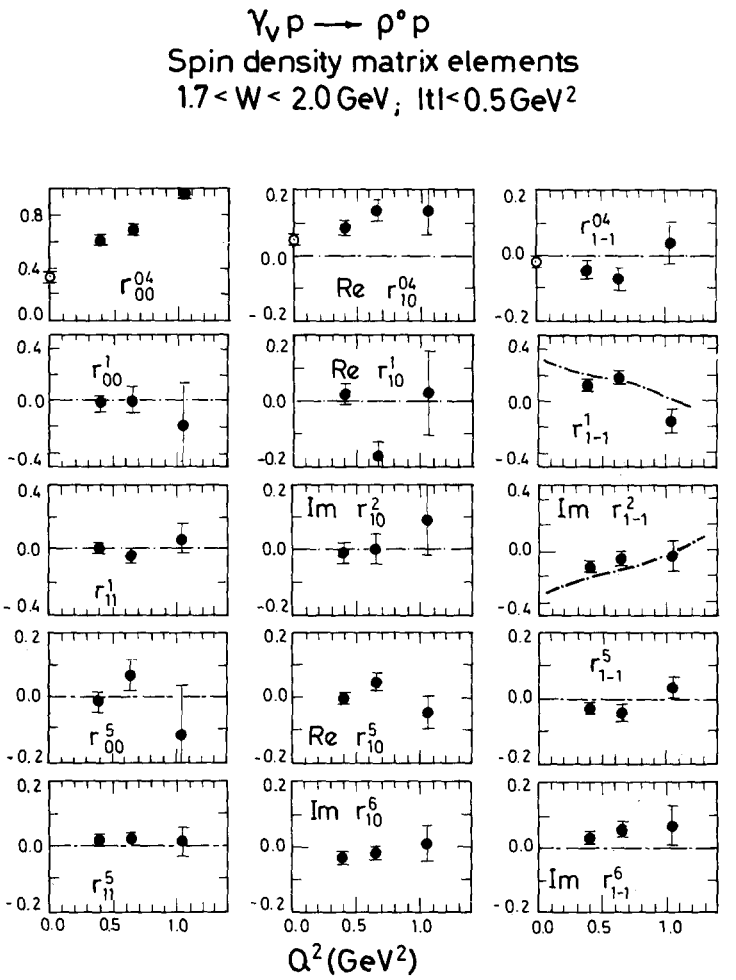

Fig. 15a.

We now discuss helicity double-flip contributions. The element r^{04}_{1-1} measures the interference between helicity non-flip and helicity *double-flip* amplitudes. From the values of r^{04}_{1-1} for $W > 2$ GeV we find (in a similar way as above) that helicity double-flip amplitudes are smaller than the helicity single-flip amplitudes.

In conclusion, ρ electroproduction for $2.1 < W < 2.8$ GeV and $Q^2 < 1.4$ GeV^2 is dominated by SCHC-amplitudes. The limits on the helicity-single-flip amplitudes are larger than those found in photoproduction.

(iii) The ratio $R = \sigma_L/\sigma_T$

Assuming SCHC, longitudinal rhos are produced by longitudinal photons only, and transverse rhos by transverse photons only. The ratio $R = \sigma_L/\sigma_T$ of the respective cross

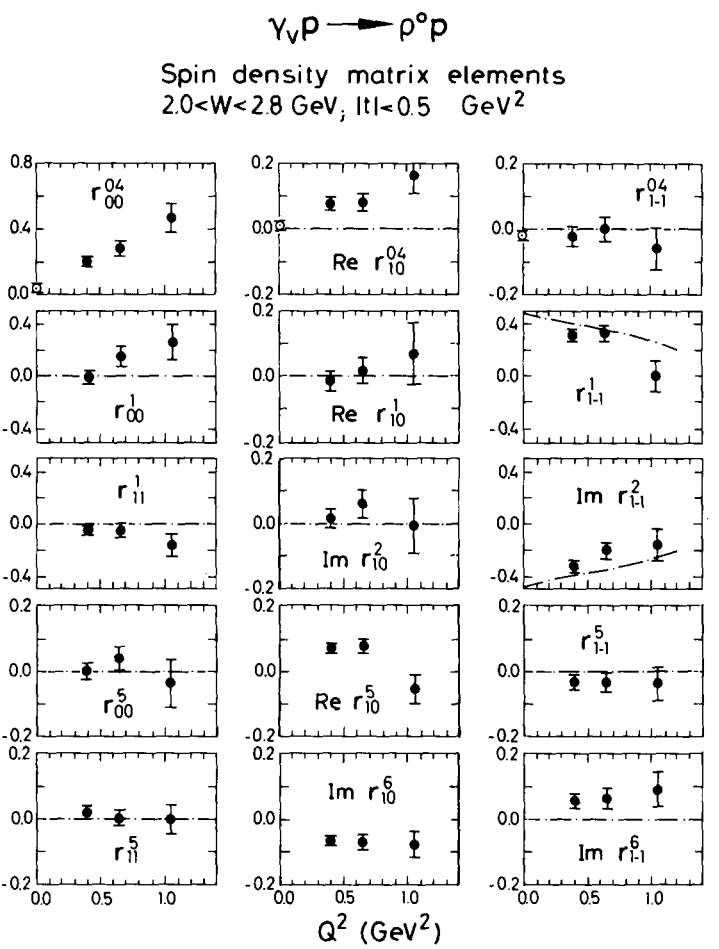

Fig. 15b.

Fig. 15. Same as fig. 14, but as a function of Q^2 for (a) $1.7 < W < 2.0$ GeV. (b) $2.0 < W < 2.8$ GeV.

Table 7
$R = \sigma_L/\sigma_T$ for $\gamma_V p \to \rho^0 p$ as a function of W and Q^2 ($|t| < 0.5$ GeV^2)

W (GeV)	Q^2 (GeV^2)		
	0.3–0.5	0.5–0.8	0.8–1.4
1.7–1.9	1.97 ± 0.35	2.85 ± 0.85	
1.9–2.1	0.73 ± 0.14	1.44 ± 0.42	2.29 ± 1.64
2.1–2.4	0.23 ± 0.07	0.39 ± 0.13	1.01 ± 0.51
2.4–2.8	0.21 ± 0.09	0.34 ± 0.14	0.95 ± 0.56

sections can then be calculated directly from r_{00}^{04}:

$$R = \frac{1}{\epsilon} \frac{r_{00}^{04}}{1 - r_{00}^{04}} , \tag{16}$$

where ϵ is the polarization parameter.

Fig. 16a,b and table 7 show R *versus* Q^2 for different regions of W as determined

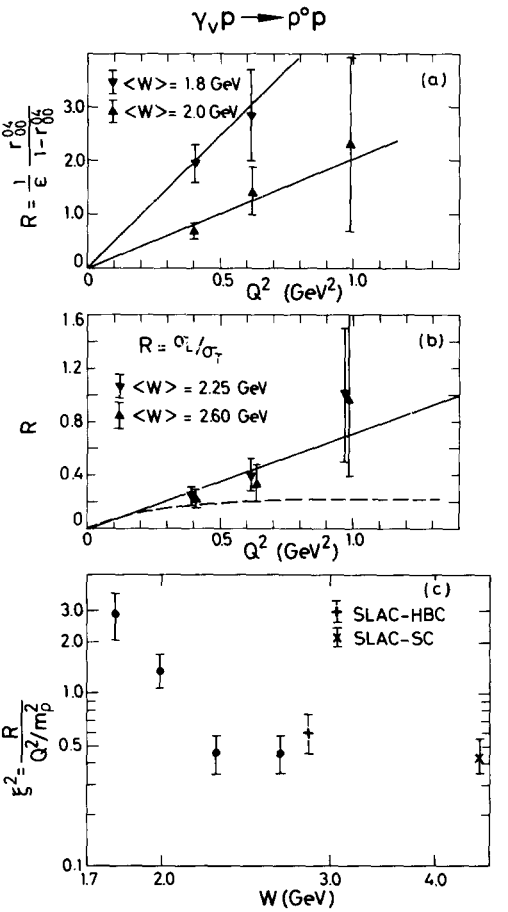

Fig. 16. Reaction $\gamma_V p \to \rho^0 p$ for $|t| < 0.5$ GeV^2. (a), (b) $R = r_{00}^{04}/\epsilon(1 - r_{00}^{04})$ as a function of Q^2 for different W intervals. The full lines are fits to $R = \xi^2 Q^2/M_\rho^2$. The dotted line represents $R = \sigma_L^{tot}/\sigma_T^{tot}$ from ref. [22]. (c) The slope ξ^2 as a function of W. The points labelled SLAC-SC and SLAC-HBC are taken from refs. [16] and [17], respectively.

by eq. (16). R is seen to rise linearly with Q^2 (for $Q^2 \leqslant 1.4$ GeV^2) *. Note that σ_L and therefore R has to vanish at $Q^2 = 0$. The available data are well represented by the following parametrization (see straight lines in fig. 16a and b)

$$R = \xi^2 \, Q^2/M_\rho^2 \, , \tag{17}$$

with ξ^2 being constant above $W = 2$ GeV and of the order of 0.5. The dashed line in fig. 16b gives the ratio $R = \sigma_L^{tot}/\sigma_T^{tot}$ for total inelastic electroproduction [22]. Apparently the contributions from longitudinal photons are smaller in the total inelastic $\gamma_V p$ cross section than in ρ production. The values of ξ^2 resulting from the parametrization (17) are shown in fig. 16c. For comparison we give the results from other experiments [16,17]; ξ^2 is 0.4–0.5 in the W range 2–5 GeV.

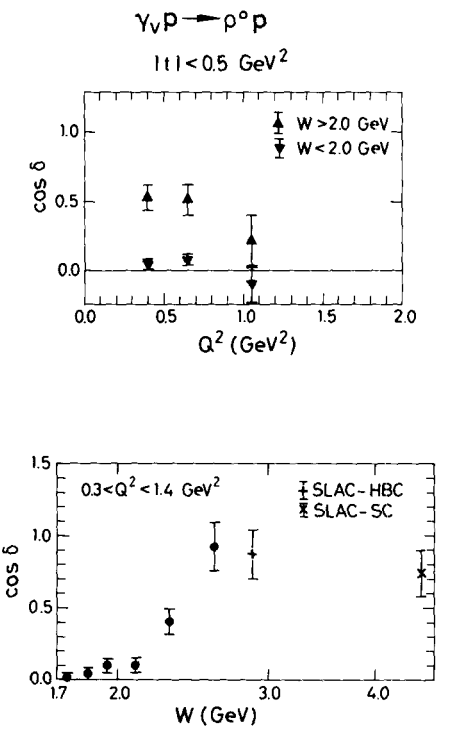

Fig. 17. Cos δ (phase between longitudinal and transverse amplitudes) as a function of W and Q^2 for $|t| < 0.5$ GeV^2. The points labelled SLAC-SC and SLAC-HBC are from refs. [16] and [17], respectively.

* The R values calculated for $W \leqslant 2$ GeV should be taken with caution since the assumption of SCHC might not be satisfied at these low energies as indicated by the lack of SCHC in ρ photoproduction near threshold.

Table 8
Cos δ as a function of W and Q^2 for $|t| < 0.5$ GeV^2

$\langle W \rangle$ (GeV)	cos δ	
1.75	0.017 ± 0.036	$0.3 < Q^2 < 1.4$ GeV^2
1.85	0.038 ± 0.044	
1.95	0.096 ± 0.051	
2.10	0.100 ± 0.054	
2.30	0.930 ± 0.171	

$\langle Q^2 \rangle$ (GeV^2)	$1.7 < W < 2.0$ GeV	$2.0 < W < 2.8$ GeV
0.40	0.05 ± 0.03	0.53 ± 0.09
0.65	0.08 ± 0.04	0.52 ± 0.11
1.05	−0.15 ± 0.21	0.23 ± 0.22

(iv) Longitudinal-transverse interference

We now determine the phase δ between the longitudinal and transverse amplitudes T_{00} and T_{11}. Assuming SCHC and only natural parity exchange the decay distribution has the form of eq. (A.6). If cos δ ≠ 0 (i.e. the two amplitudes interfere) the last term in eq. (A.6) leads to an interference pattern in the decay distribution. For cos δ > 0 the event density should be highest near $\psi_H = 0°$ or 360° (for cos $\theta_H < 0$) and near $\psi_H = 180°$ (for cos $\theta_H > 0$). This interference pattern is observed in fig. 13 (lower scatter plot) for $W > 2$ GeV. We determine the phase δ from eq. (A.8). The resulting cos δ values are shown in fig. 17 and table 8 as functions of Q^2 and W together with the data from other experiments [16,17]. At W values around 2 GeV the two amplitudes are roughly 90° out of phase; with increasing energy the phase difference becomes smaller; above $W = 2.5$ GeV the rho production amplitudes from longitudinal and transverse photons are roughly in phase.

4.5. Comparison with VDM

The VDM prediction for the Q^2 dependence of σ_ρ is shown by the curves in fig. 8. They were calculated from the following expression [23]:

$$\sigma_{\gamma_V p \to \rho^0 p}(Q^2, W) = \frac{p^*_{in}(Q^2 = 0)}{p^*_{in}(Q^2)} \left(\frac{M_\rho^2}{M_\rho^2 + Q^2}\right)^2 \left\{1 + \epsilon\xi^2 \frac{Q^2}{M_\rho^2}\right\}$$

$$\times \sigma_{\gamma p \to \rho^0 p}(Q^2 = 0, W) \exp[A(Q^2) t_{min}(Q^2) - A(0) t_{min}(0)] , \qquad (18)$$

where p^*_{in} is the photon momentum in the hadron c.m.s., $p^*_{in}(Q^2 = 0)/p^*_{in}(Q^2) = (W^2 - m_p^2)/\{W^2 - m_p^2 - Q^2)^2 + 4W^2Q^2\}^{1/2}$.

The ratio $p^*_{in}(Q^2=0)/p^*_{in}(Q^2)$ enters eq. (18) because of the difference in photon flux for different Q^2 at a given value of W. The quantity $R = \xi^2 Q^2/M_\rho^2$ measures the ratio of the ρ production cross sections by longitudinal and transverse photons. R was taken from the analysis of the decay angular distribution assuming s-channel helicity conservation in ρ^0 production (see subsect. 4.4.2). The factor $\exp(A t_{min})$ corrects for the $|t|_{min}$ cutoff.

The VDM prediction describes the data well. We conclude from this that within VDM the product of the γ-ρ coupling constant times the ρN elastic scattering amplitude is independent of Q^2. This strongly supports the assumption that the $\gamma\rho$ coupling constant itself is independent of Q^2 which is one of the basic assumptions of VDM.

5. Conclusions

We have studied the reaction $ep \to ep\pi^+\pi^-$ in terms of the process $\gamma_V p \to p\pi^+\pi^-$ for hadron c.m.s. energies between 1.3 and 2.8 GeV and Q^2 from 0.3 to 1.4 GeV^2. The low energy region ($W < 1.7$ GeV) is dominated by $\pi^-\Delta^{++}$ production, the high energy region ($W > 2$ GeV) by $\rho^0 p$ production. With increasing Q^2 phase-space like events become important.

The following properties are observed for ρ^0 production:

(i) The rho mass shape is skewed as in photoproduction. The skewing is independent of Q^2 if the sum of transverse and longitudinal polarized rhos is considered. An analysis made separately for the two parts indicates less skewing than in photoproduction for transverse rhos at large Q^2. This evidence for a change of the transverse rho shape with Q^2 is in agreement with the Söding model.

(ii) Near threshold rho production has peripheral and nonperipheral contributions of comparable magnitude. The nonperipheral part depends only weakly on Q^2 and reduces rapidly with increasing W. The cross section for the peripheral component is approximately constant with energy as expected for a diffractive process.

(iii) At all energies the peripheral part of $\sigma(\gamma_V p \to \rho^0 p)$ reduces with Q^2 following the rho propagator as predicted by VDM.

(iv) The slope of the differential cross section, $d\sigma/dt$, measured at $\langle Q^2 \rangle = 0.4$ and 0.8 GeV^2 is within errors equal to its value at $Q^2 = 0$; i.e. we have no evidence for a flattening of the t distribution, which would correspond to a "shrinking" photon.

(v) The ρ^0 decay angular distribution in the helicity system shows longitudinal rho mesons dominating in the threshold region ($r^{04}_{00} \simeq 0.7$). At higher energies transversely polarized rhos dominate ($r^{04}_{00} = 0.25 \pm 0.04$ for $\langle W \rangle = 2.45$ GeV, $\langle Q^2 \rangle = 0.6$ GeV^2). However the fraction of longitudinal rhos rises linearly with increasing Q^2.

(vi) The ρ^0 density matrix shows that transverse rho mesons are produced by natural parity exchange in the t-channel: $\sigma^N_T(\gamma_V p \to \rho^0 p) \geqslant (0.83 \pm 0.06)\sigma_T(\gamma_V p \to \rho^0 p)$ for $\langle W \rangle = 2.45$ GeV, $\langle Q^2 \rangle = 0.65$ GeV^2. Furthermore, the production mechanism conserves approximately s-channel helicity at the photon vertex (SCHC). Assuming

SCHC the ratio $R = \sigma_L/\sigma_T$ has been calculated from the value of r_{00}^{04}. The Q^2 dependence of R can be parametrized by a linear form, $R = \xi^2 Q^2/M_\rho^2$ with $\xi^2 = 0.4$ for $W > 2$ GeV, i.e. $\sigma_L \approx \sigma_T$ near $Q^2 \simeq 1.4$ GeV^2.

(vii) For $W > 2.2$ GeV the density matrix shows the presence of interference between the amplitudes for rho production by longitudinal and transverse photons. Assuming SCHC and only natural parity exchange, the phase δ between the two amplitudes can be calculated. The result is $\cos\delta \approx 0$ below $W = 2$ GeV (i.e. no interference) and $\cos\delta = 0.52 \pm 0.09$ for $\langle W\rangle = 2.45$ GeV, $\langle Q^2\rangle = 0.5$ GeV^2 and $|t| < 0.5$ GeV^2. With increasing energy the relative phase decreases, a behaviour which is expected if both production processes become diffractive.

In summary, in the range $W > 2$ GeV and $Q^2 < 1.4$ GeV^2 which corresponds to values of the scaling variable $\omega \gtrsim 5$ the observed properties of rho electroproduction resemble those of rho photoproduction and are consistent with a dominantly diffractive production mechanism.

We thank I.J. Bloodworth, B. Naroska, D. Notz and W.J. Podolsky for their contributions in the early stages of this experiment. We are indebted to N. Gollmer, E. Hell, V. Heynen, A.Huber, K. Klinkmüller, G. Kraft, H.H. Sabath, H.W. Sass, K. Westphal and K.H. Wroblewski for technical assistance. The excellent performance of the Synchrotron crew, of the Hallendienst and of the Kältetechnik is gratefully acknowledged. We want to thank our scanning and measuring personnel for their careful work. The cooperation by Mr. Kuhlmann and the Rechenzentrum has been very helpful.

The work at Hamburg has been supported by the Bundesministerium für Forschung und Technologie. The work at Glasgow has been supported by the Science Research Council.

Appendix

Decay angular distributions and density matrix formalism

A.1. Definition of angles

The ρ^0 decay is analyzed in the s-channel helicity system with the ρ^0 direction in the overall hadron c.m.s. taken as the quantization axis. The ρ decay angles θ_H, ϕ_H are calculated from the unit vectors $\hat{k}, \hat{p}', \hat{q}, \hat{\pi}^+$ pointing along the direction of the virtual photon, the scattered proton, the rho and the π^+ from rho decay respectively

$$\cos\theta_H = (\hat{q}\cdot\hat{\pi}^+),$$

$$\cos\phi_H = \frac{(\hat{k}\times\hat{q})\cdot(\hat{q}\times\hat{\pi}^+)}{|\hat{k}\times\hat{q}|\cdot|\hat{q}\times\hat{\pi}^+|},$$

$$\sin\phi_H = \frac{-[(\hat{k}\times\hat{q})\times\hat{q}]\cdot(\hat{q}\times\hat{\pi}^+)}{|(\hat{k}\times\hat{q})\times\hat{q}|\cdot|\hat{q}\times\hat{\pi}^+|}.$$

Here, all vectors are to be calculated in the ρ^0 *rest frame*, with $\hat{q}$ defined to be $-\hat{p}'$. We also use the angle Φ of the polarization vector of the transverse photons in the hadron c.m.s., which is given by the angle between the ρ production plane and the electron scattering plane:

$$\cos\Phi = \frac{(\hat{k}\times\hat{q})\cdot(\hat{e}\times\hat{e}')}{|\hat{k}\times\hat{q}|\cdot|\hat{e}\times\hat{e}'|},$$

$$\sin\Phi = \frac{[(\hat{k}\times\hat{q})\times(\hat{e}\times\hat{e}')]\cdot\hat{k}}{|\hat{k}\times\hat{q}|\cdot|\hat{e}\times\hat{e}'|}.$$

All vectors are to be taken in the *hadron c.m.s.*; $\hat{e}$ and $\hat{e}'$ are unit vectors pointing in the direction of the incident and the scattered electron.

A.2. Density matrix formalism

We analyze the ρ^0 decay angular distribution $W(\cos\theta_H, \phi_H, \Phi)$ in terms of the ρ^0 density matrix in the helicity system using the formalism of ref. [14]. The ρ^0 density matrix, ρ_{ik}, in general, can be decomposed into six independent matrices ρ^α_{ik}, where the matrices for $\alpha = 0$–2 and 4 describe ρ^0 production by transverse and longitudinal photons, respectively *; the matrices for $\alpha = 5$–6 measure transverse/longitudinal interference terms. When, as in this experiment, the ratio of the longitudinal to transverse photon flux as measured by ϵ is not varied, the contributions from ρ^0 and ρ^4 cannot be separated and $W(\cos\theta, \phi, \Phi)$ ** measures certain combinations of the ρ^α_{ik}:

$$r^{04}_{ik} = \frac{\rho^0_{ik} + \epsilon R\rho^4_{ik}}{1+\epsilon R}, \tag{A.1}$$

$$r^\alpha_{ik} = \frac{\rho^\alpha_{ik}}{1+\epsilon R}, \qquad \alpha = 1\text{–}2, \tag{A.2}$$

$$r^\alpha_{ik} = \frac{\sqrt{R}\,\rho^\alpha_{ik}}{1+\epsilon R}, \qquad \alpha = 5\text{–}6, \tag{A.3}$$

where $R = \sigma_L/\sigma_T$ is the ratio of the cross sections for rho production by longitudinal and transverse photons. Note that as $Q^2 \to 0$, $r^{04}_{ik} \to \rho^0_{ik}$ and $r^\alpha_{ik} \to \rho^\alpha_{ik}$ ($\alpha = 1$–2). The decay distribution in terms of the r^α_{ik} reads (ref. [14]):

$$W(\cos\theta,\phi,\Phi) = \frac{3}{4\pi}\,[\tfrac{1}{2}(1-r^{04}_{00}) + \tfrac{1}{2}(3r^{04}_{00}-1)\cos^2\theta$$
$$-\sqrt{2}\,\mathrm{Re}\,r^{04}_{10}\sin 2\theta\cos\phi - r^{04}_{1-1}\sin^2\theta\cos 2\phi - \epsilon\cos 2\Phi\{r^1_{11}\sin^2\theta$$

* With longitudinally polarized electrons additional terms ρ^3_{ik}, ρ^7_{ik} and ρ^8_{ik} enter.

** In the following we omit the subscript H of the decay angles in the helicity system.

$$+ r^1_{00}\cos^2\theta - \sqrt{2}\,\mathrm{Re}\,r^1_{10}\sin 2\theta\cos\phi - r^1_{1-1}\sin^2\theta\cos 2\phi\}$$

$$- \epsilon\sin 2\Phi\{\sqrt{2}\,\mathrm{Im}\,r^2_{10}\sin 2\theta\sin\phi + \mathrm{Im}\,r^2_{1-1}\sin^2\theta\sin 2\phi\}$$

$$+ \sqrt{2\epsilon(1+\epsilon)}\cos\Phi\{r^5_{11}\sin^2\theta + r^5_{00}\cos^2\theta - \sqrt{2}\,\mathrm{Re}\,r^5_{10}\sin 2\theta\cos\phi$$

$$- r^5_{1-1}\sin^2\theta\cos 2\phi\} + \sqrt{2\epsilon(1+\epsilon)}\sin\Phi\{\sqrt{2}\,\mathrm{Im}\,r^6_{10}\sin 2\theta\sin\phi$$

$$+ \mathrm{Im}\,r^6_{1-1}\sin^2\theta\sin 2\phi\}] \,. \tag{A.4}$$

If the s-channel helicity is conserved (SCHC) at the $\gamma\rho$ vertex all matrix elements except r^{04}_{00}, r^1_{1-1}, $\mathrm{Im}\,r^2_{1-1}$, $\mathrm{Re}\,r^5_{10}$, $\mathrm{Im}\,r^6_{10}$ are zero. Furthermore $r^1_{1-1} = -\mathrm{Im}\,r^2_{1-1}$ and $\mathrm{Re}\,r^5_{10} = -\mathrm{Im}\,r^6_{10}$ (see appendix A of ref. [14] for an explicit expression of the density matrices in terms of helicity amplitudes). In this case eq. (A.4) reduces to

$$W(\cos\theta,\psi) = \frac{3}{4\pi}\,[\tfrac{1}{2}(1 - r^{04}_{00}) + \tfrac{1}{2}(3r^{04}_{00} - 1)\cos^2\theta$$

$$+ \epsilon r^1_{1-1}\sin^2\theta\cos 2\psi - 2\sqrt{\epsilon(1+\epsilon)}\,\mathrm{Re}\,r^5_{10}\sin 2\theta\cos\psi] \,. \tag{A.5}$$

Here we used the polarization angle $\psi = \phi - \Phi$. The term $\sin^2\theta\cos 2\psi$ characterises transverse rhos while contributions from longitudinal rhos have $\cos^2\theta$ distributions and no ψ dependence.

Assuming SCHC and only natural parity exchange the decay distribution (A.5) reduces further to (see sect. 5 of ref. [14])

$$W(\cos\theta,\psi) = \frac{1}{1+\epsilon R}\,\frac{3}{8\pi}\,\{\sin^2\theta\,(1 + \epsilon\cos 2\psi) + 2\epsilon R\cos^2\theta$$

$$- \sqrt{2\epsilon(1+\epsilon)R}\,\cos\delta\sin 2\theta\cos\psi\} \,. \tag{A.6}$$

δ is the phase between the longitudinal and transverse photon amplitudes T_{00} and T_{11} defined by

$$T_{00}T^*_{11} = |T_{00}|\,|T_{11}|\,\mathrm{e}^{-i\delta} \,. \tag{A.7}$$

The $T_{\lambda_\rho\lambda_\gamma}$ are helicity amplitudes for rho and photon helicities λ_ρ and λ_γ with a summation over the nucleon helicities implied; $\cos\delta$ can be expressed by the r_{ik} *via*

$$\cos\delta = \frac{1+\epsilon R}{\sqrt{R/2}}\,(\mathrm{Re}\,r^5_{10} - \mathrm{Im}\,r^6_{10}) \,, \tag{A.8}$$

with

$$R = \frac{1}{\epsilon}\,\frac{r^{04}_{00}}{1 - r^{04}_{00}} \,. \tag{A.9}$$

According to eq. (A.9) the ratio $R = \sigma_L/\sigma_T$ is determined by the matrix element r^{04}_{00} (in case of SCHC).

A.3. s-channel helicity conservation

We can estimate the size of helicity single-flip contributions from the value of Re r^{04}_{10}. According to eq. (A.1), Re r^{04}_{10} is given by

$$\text{Re}\, r^{04}_{10} = \frac{\text{Re}\, \rho^0_{10} + \epsilon R\, \text{Re}\, \rho^4_{10}}{1 + \epsilon R} \,. \tag{A.10}$$

The density matrices $\rho^0_{\lambda\lambda'}$ and $\rho^4_{\lambda\lambda'}$ are related to the helicity amplitudes $T_{\lambda_p \lambda_\gamma}$ in the following way (see appendix A of ref. [14]):

$$\rho^0_{\lambda\lambda'} = \frac{1}{2N_T} \sum_{\lambda_\gamma = \pm 1} T_{\lambda\lambda_\gamma} T^*_{\lambda'\lambda_\gamma} \quad \text{with} \quad N_T = \tfrac{1}{2} \sum_{\lambda,\lambda_\gamma = \pm 1} |T_{\lambda\lambda_\gamma}|^2 \,, \tag{A.11}$$

$$\rho^4_{\lambda\lambda'} = \frac{1}{N_L}\, T_{\lambda 0} T^*_{\lambda' 0} \qquad \text{with} \quad N_L = \sum_{\lambda} |T_{\lambda 0}|^2 \,. \tag{A.12}$$

Hence

$$\rho^0_{10} = \frac{T_{11}T^*_{01} + T_{-11}T^*_{0\text{-}1}}{(|T_{11}|^2 + |T_{\text{-}1\text{-}1}|^2 + |T_{1\text{-}1}|^2 + |T_{\text{-}11}|^2)} \,,$$

$$\rho^4_{10} = \frac{T_{10}T^*_{00}}{|T_{10}|^2 + |T_{00}|^2 + |T_{\text{-}10}|^2}$$

We assume that the helicity flip amplitudes are small and neglect the products of two helicity flip amplitudes. Then (A.10) reads

$$\text{Re}\, r^{04}_{10} = \frac{\text{Re}\,(T_{11}T^*_{01})}{2(1+\epsilon R)\,|T_{11}|^2} + \frac{\epsilon R}{1+\epsilon R}\, \frac{\text{Re}\,(T_{10}\,T^*_{00})}{|T_{00}|^2} \,. \tag{A.13}$$

If the helicity flip and the non-flip amplitudes are in phase we obtain

$$\text{Re}\, r^{04}_{10} = \frac{1}{2(1+\epsilon R)}\, \frac{|T_{01}|}{|T_{11}|} + \frac{\epsilon R}{1+\epsilon R}\, \frac{|T_{10}|}{|T_{00}|} \,. \tag{A.14}$$

We finally assume

$$\frac{|T_{01}|}{|T_{11}|} = \frac{|T_{10}|}{|T_{00}|} = \frac{|T_{\text{flip}}|}{|T_{\text{non-flip}}|} \,,$$

i.e. the ratio of helicity single-flip to helicity non-flip contributions to be the same for longitudinal and transverse photons. Then

$$\mathrm{Re}\, r_{10}^{04} = \frac{|T_{\mathrm{flip}}|}{|T_{\mathrm{non\text{-}flip}}|} \frac{1 + 2\epsilon R}{2(1 + \epsilon R)} \tag{A.15}$$

References

[1] V. Eckardt et al., Phys. Letters 43B (1973) 240; Nuovo Cimento Letters 6 (1973) 551.
[2] V. Eckardt et al., Nucl. Phys. B55 (1973) 45;
E. Rabe, Thesis, Internal report DESY F1-74/2 (1974), unpublished.
[3] V. Eckardt et al., DESY report 74/5 (1974), unpublished.
[4] P. Joos et al., Phys. Letters 52B (1974) 481.
[5] C. Sander, Diploma thesis, Internal report DESY F1-75/3 (1975), unpublished.
[6] CERN TC-Library.
[7] L.Y. Mo and Y.S. Tsai, Rev. Mod. Phys. 41 (1969) 205.
[8] K. Wacker, Thesis, Internal report DESY F1-76/04 (1976), unpublished.
[9] S. Stein et al., Phys. Rev. D12 (1975) 1884.
[10] L. Hand, Phys. Rev. 129 (1964) 1834.
[11] ABBHHM Collaboration, Phys. Rev. 175 (1968) 1669.
[12] H. Spitzer, DESY Internal report F1-71/4 (1971), unpublished.
[13] MURTLEBERT, J. Friedman, Alvarez Group Programming Note No. P-156 (1966), Lawrence Radiation Laboratory, Berkeley, unpublished.
[14] K. Schilling and G. Wolf, Nucl. Phys. B61 (1973) 381.
[15] J. Ballam et al., Phys. Rev. D5 (1972) 545.
[16] J. Dakin et al., Phys. Rev. D8 (1973) 687.
[17] J. Ballam et al., Phys. Rev. D10 (1974) 765.
[18] R.F. Mozley, SLAC-PUB-1671 (1975);
B. Lieberman, Thesis, University of California at Santa Cruz, USA (1975).
[19] P. Söding, Phys. Letters 19 (1965) 702.
[20] L. Ahrens et al., Phys. Rev. D9 (1974) 1894.
[21] H. Cheng and T.T. Wu, Phys. Rev. 183 (1969) 1324;
J.D. Bjorken, J. Kogut and D. Soper, Phys. Rev. D2 (1971) 1382;
H.T. Nieh, Phys. Letters 38B (1972) 100.
[22] E.M. Riordan et al., SLAC-PUB-1634 (1975).
[23] H. Fraas and D. Schildknecht, Nucl. Phys. B14 (1969) 543.